

# EQUIPARTITION GAMMA-RAY BLAZARS AND THE LOCATION OF THE GAMMA-RAY EMISSION SITE IN 3C 279

CHARLES D. DERMER<sup>1</sup>, MATTEO CERRUTI<sup>2,3</sup>, BENOIT LOTT<sup>4</sup>, CATHERINE BOISSON<sup>3</sup>, ANDREAS ZECH<sup>3</sup>

*Draft version February 27, 2024*

## ABSTRACT

Blazar spectral models generally have numerous unconstrained parameters, leading to ambiguous values for physical properties like Doppler factor  $\delta_D$  or fluid magnetic field  $B'$ . To help remedy this problem, a few modifications of the standard leptonic blazar jet scenario are considered. First, a log-parabola function for the electron distribution is used. Second, analytic expressions relating energy loss and kinematics to blazar luminosity and variability, written in terms of equipartition parameters, imply  $\delta_D$ ,  $B'$ , and the peak electron Lorentz factor  $\gamma'_{pk}$ . The external radiation field in a blazar is approximated by Ly $\alpha$  radiation from the broad line region (BLR) and  $\approx 0.1$  eV infrared radiation from a dusty torus. When used to model 3C 279 SEDs from 2008 and 2009 reported by Hayashida et al. (2012), we derive  $\delta_D \sim 20 - 30$ ,  $B' \sim \text{few G}$ , and total (IR + BLR) external radiation field energy densities  $u \sim 10^{-2} - 10^{-3}$  erg cm<sup>-3</sup>, implying an origin of the  $\gamma$ -ray emission site in 3C 279 at the outer edges of the BLR. This is consistent with the  $\gamma$ -ray emission site being located at a distance  $R \lesssim \Gamma^2 c t_{var} \sim 0.1(\Gamma/30)^2 (t_{var}/10^4 \text{ s})$  pc from the black hole powering 3C 279's jets, where  $t_{var}$  is the variability time scale of the radiation in the source frame, and at farther distances for narrow-jet and magnetic-reconnection models. Excess  $\gtrsim 5$  GeV  $\gamma$ -ray emission observed with Fermi LAT from 3C 279 challenge the model, opening the possibility of non-leptonic and hadronic origin of the emission. For low hadronic content, absolute jet powers of  $\approx 10\%$  of the Eddington luminosity are calculated.

*Subject headings:* Gamma rays: general – Galaxies: jets – radiation mechanisms: nonthermal

## 1. INTRODUCTION

The time-varying emission spectrum of a blazar encodes important information about particle acceleration and radiation, jet structure and environment, and the mechanisms by which black holes power jets. Determining the jet physics and environment from the spectral energy distributions (SEDs) of blazars is a tricky problem of inversion. Part of the problem is that observational limitations make it difficult to obtain a detailed picture of the blazar SED, as the blazar continuum extends over some 20 orders of magnitude from MHz radio frequencies to TeV  $\gamma$ -ray energies, and therefore requires coordinated campaigns at many wavelengths. The observing program furthermore has to be as nearly simultaneous as possible, due to the highly variable nature of blazars. In spite of these obstacles, extraordinary progress has been made to obtain a relatively complete description of the blazar SED.

Here we introduce a new model of blazar SEDs, built on the principle of equipartition. We use the 3C 279 data in Hayashida et al. (2012) from which to make a test of the model. But first we give background.

The EGRET instrument on the *Compton* Gamma Ray

Observatory first showed that 100 MeV – GeV emission often dominates the apparent power output of blazars during flaring states of flat spectrum radio quasars (FSRQs), and that the  $\gamma$  rays form a spectral component that is distinct from the nonthermal synchrotron emission radiated at radio, IR and optical frequencies (see, e.g., Hartman et al. 1992; Wehrle et al. 1998). The ground-based Cherenkov  $\gamma$ -ray telescopes demonstrated that the BL Lac class are powerful sources of TeV emission (Punch et al. 1992), and that FSRQs, including 3C 279 (MAGIC Collaboration 2008) at redshift  $z = 0.5362$  (Marziani et al. 1996), PKS 1510-089 ( $z = 0.36$ ) (Wagner et al. 2010; Cortina 2012; Abramowski et al. 2013), and 4C +21.35 (PKS 1222+216;  $z = 0.432$ ) (Aleksić et al. 2011), are sources of very-high energy (VHE;  $\gtrsim 100$  GeV)  $\gamma$  rays.

The Large Area Telescope (LAT) on *Fermi*, which nominally operates in scanning mode, has revolutionized our understanding of blazars by providing uninterrupted light curves and detailed SEDs of blazars. In campaigns involving radio, IR, optical, X-ray, and ground-based  $\gamma$ -ray telescopes, superbly detailed SEDs have been measured that challenge our theoretical understanding. A few examples include the high-synchrotron-peaked BL Lacs Mrk 421 (Abdo et al. 2011b) and Mrk 501 (Abdo et al. 2011c), the intermediate synchrotron-peaked BL Lac 3C 66A (Abdo et al. 2011d), and the FSRQs 3C 454.3 (Abdo et al. 2009) and 3C 279 (Abdo et al. 2010a). Mrk 421 and Mrk 501 are reasonably well fit with a leptonic synchrotron/SSC model, whereas an additional  $\gamma$ -ray component, thought to arise from Compton scattering of external radiation fields, is required in FSRQs and low- and intermediate synchrotron-peaked BL Lac objects.

<sup>1</sup> Code 7653, Space Science Division, U.S. Naval Research Laboratory, Washington, DC 20375, USA. e-mail: charles.dermer@nrl.navy.mil

<sup>2</sup> Harvard-Smithsonian Center for Astrophysics; 60 Garden Street, 02138 Cambridge, MA, USA. email: matteo.cerruti@cfa.harvard.edu

<sup>3</sup> Laboratoire Univers et Théories (LUTH), Observatoire de Paris-Meudon, 5 Place Jules Janssen 92195 Meudon Cedex, France.

<sup>4</sup> Centre d'Études Nucléaires Bordeaux Gradignan, Université de Bordeaux, CNRS/IN2P3, UMR 5797, Gradignan, 33175, France

A standard blazar paradigm consisting of magnetized plasma ejected with relativistic speeds in a collimated outflow along the polar axes of a rotating black hole has been developed to explain the overall observational features of blazars (see Böttcher et al. 2012, for a recent detailed review). But even the simple synchrotron/SSC model suffers from a proliferation of parameters, which greatly increases with the introduction of external radiation fields having an uncertain spectrum and energy density. The range of possible fits to the SEDs makes it difficult to extract unique and therefore meaningful blazar jet properties. Part of this difficulty has to do with characterizing the nonthermal electron spectrum, and another part with the range of possibilities for the sources of target photons, which can include the accretion-disk (Dermer et al. 1992; Dermer & Schlickeiser 1993; Dermer & Schlickeiser 2002), broad line region (BLR; Sikora et al. 1994), and molecular torus (Błażejowski et al. 2000; Arbeiter et al. 2002; Sokolov & Marscher 2005) (see also Böttcher 2007; Sikora et al. 2009).

To help alleviate these problems, we adopt a specific model of the electron distribution and assume that the primary target radiation fields are (i) the BLR atomic-line radiation, and (ii) the IR radiation from a dusty torus surrounding the nucleus. We employ a log-parabola function in Section 2 to describe the electron energy distribution in the comoving fluid frame. Equipartition relations between the energy densities of the magnetic field, the nonthermal electrons, and the observed properties of the blazar synchrotron spectrum are derived in Section 3. In Section 4, model results are shown for target photons of the external radiation described by monochromatic frequencies and various energy densities. In Section 5, spectral fitting of recent SEDs of 3C 279 (Hayashida et al. 2012) are used to illustrate the method. Discussion of results is found in Section 6.

In a companion paper (Cerruti et al. 2013), we improve the model for the external radiation field, replacing monochromatic infrared emission by thermal spectra, and the BLR radiation field by a complex of atomic emission lines rather than by the Ly $\alpha$  line alone. We show that scattering of the BLR radiation under equipartition conditions can explain the GeV spectral cutoff discovered with *Fermi*-LAT in 3C 454.3 and other FSRQs and low- and intermediate-synchrotron-peaked BL Lac objects (Abdo et al. 2009, 2010b).

## 2. LOG-PARABOLA ELECTRON DISTRIBUTION

In leptonic blazar jet models, the synchrotron and Compton  $\gamma$ -ray emission components are radiated by nonthermal electron distributions that are assumed to be isotropic in the jet fluid frame. One technique is to fit the data by injecting power-law particle distributions and allowing the particles to evolve in response to radiative and adiabatic energy losses (e.g., Böttcher & Chiang 2002; Moderski et al. 2003; Katarzyński et al. 2003). Many parameters must be specified, including the cutoff energies, injection indices, and power, but this method is potentially useful to follow the dynamic spectral behavior of blazars.

Contrary to this approach, we abandon any preconceptions about particle acceleration, and employ the simplest functional form that is able to provide reasonably

good fits to the snapshot SED data (compare Finke et al. 2008, for SSC modeling of TeV blazars with power-law electron distributions.). For this purpose, we assume that the log-parabola function

$$\log[\gamma'^2 N'_e(\gamma')] = \log[\gamma_{pk}'^2 N_e(\gamma_{pk}')] - b \log(\gamma'/\gamma_{pk}')^2 \quad (1)$$

gives a good description of the nonthermal electron Lorentz-factor ( $\gamma'$ ) distribution  $N'_e(\gamma')$  in the comoving fluid frame, where the electron distribution is assumed to be isotropic. The entire description of the electron energy distribution is then given by three parameters: the normalization, the peak Lorentz factor  $\gamma'_{pk}$ , and the spectral curvature parameter  $b$ . Electrons with  $\gamma' \approx \gamma'_{pk}$  therefore contain the maximum nonthermal electron energy per unit logarithmic interval  $\Delta(\log \gamma')$  in the electron distribution. Thus

$$\begin{aligned} \gamma'^2 N'_e(\gamma') &= \gamma_{pk}'^2 N_e(\gamma_{pk}') \left(\frac{\gamma'}{\gamma_{pk}'}\right)^{-b \log(\frac{\gamma'}{\gamma_{pk}'})} \\ &\equiv K y^{-b \log y} = K y^{-\hat{b} \ln y}, \end{aligned} \quad (2)$$

where  $y \equiv \gamma'/\gamma'_{pk}$ , and  $\hat{b} = b/\ln 10$ . The electron distribution function is a smoothly curving function with continuously varying spectral index. Normalizing to the total comoving nonthermal electron energy  $\mathcal{E}'_e$  through  $\mathcal{E}'_e = m_e c^2 \int_1^\infty d\gamma' \gamma' N'_e(\gamma')$  gives  $\mathcal{E}'_e \cong m_e c^2 \gamma_{pk}'^2 N_e(\gamma_{pk}') I(b)$ , so

$$K = \frac{\mathcal{E}'_e}{m_e c^2 I(b)}, \quad (3)$$

where  $I(b) = \sqrt{\pi \ln 10/b}$  ( $\cong 2.69/\sqrt{b}$ ). Note that the relationship is not exact, because we have replaced  $1/\gamma'_{pk}$  with 0 in the lower limit of the integral (see Appendix for error estimate and Section 6.3 for more detail on the log-parabola function and particle acceleration.).<sup>5</sup>

## 3. EQUIPARTITION RELATIONS

The principle of equipartition is attractive by providing a minimum power solution on the emissions from the jets of blazars that already demand extreme powers and large energies. In the black-hole jet system, the particle-field relations depend on uncertain jet-formation, particle acceleration and radiation mechanisms, for example, whether the jet power is provided by accretion or black-hole rotation, and whether the jet plasma is particle or field dominated. We avoid poorly understood microphysics by assuming that a condition of equipartition holds between magnetic-field and nonthermal electron energy densities, as used in the analysis of a wide variety of astrophysical systems; see Pacholczyk (1970) for a study of radio sources, and Beck & Krause (2005) for a more recent review. Note that there is large uncertainty in the “equipartition magnetic field” if it is instead coupled to the poorly known baryon content of the system. In practical terms, the principle of equipartition

<sup>5</sup> This solution neglects a larger class of solutions that are not symmetric in  $y \rightarrow 1/y$ . This deficiency can be partly mitigated by using separate low-energy ( $y \leq 1$ ) and high-energy ( $y > 1$ ) width parameters. We do the symmetrical case here, reserving the mixed case for separate study.

limits the analysis to a manageable scope by eliminating a parameter connecting the magnetic-field and lepton energy densities.

One goal is to determine, by comparison with blazar SED data, whether the synchrotron and  $\gamma$ -ray spectra are reasonably well fit by a log-parabola function for the electron energy distribution, within the scenario that the blazar jet is described by a standard relativistic jet model with quasi-isotropic electrons trapped in a randomly oriented magnetic field with mean strength  $B'$  in the fluid frame. The peak comoving electron Lorentz factor  $\gamma'_{pk}$  may represent the minimum Lorentz factor in a fast-cooling blast-wave scenario or the cooling Lorentz factor in a slow-cooling scenario (Sari et al. 1998), or the value obtained by balancing acceleration and radiative cooling. See also Ghisellini et al. (1996).

### 3.1. Parameters and derived quantities

In the stationary (source) frame of the black-hole/jet system, we can list the important observables that characterize the blazar SED:

1.  $\nu L_\nu^{pk, syn}$ , the maximum value of the nonthermal synchrotron  $\nu L_\nu$  spectrum. For a log-parabola synchrotron spectrum, the apparent isotropic bolometric synchrotron luminosity  $L_{syn} = 10^{48} L_{48} \text{ erg s}^{-1}$  is related to  $\nu L_\nu^{pk, syn}$  by Equation (B5);
2.  $\epsilon_s = h\nu_s/m_e c^2 = 8.09 \times 10^{-7} \nu_{14}$ , the peak synchrotron frequency, that is, the frequency at which the  $\nu L_\nu$  synchrotron spectrum reaches its maximum value, in units of  $m_e c^2$ , where  $10^{14} \nu_{14} \text{ Hz}$  is the peak synchrotron frequency in the source frame;
3.  $t_{var} = 10^4 t_4 \text{ s}$ , the variability time scale, where  $t_{var} = t_v^{obs}/(1+z)$ , and  $t_v^{obs}$  is the minimum measured variability time scale, and we implicitly assume a roughly cospatial origin of the nonthermal radiation components (one-zone approximation);
4.  $\nu L_\nu^{pk, C}$ , the maximum value of the nonthermal Compton  $\nu L_\nu$  spectrum. The Compton-dominance factor  $A_C \cong \nu L_\nu^{pk, C}/\nu L_\nu^{pk, syn} \cong L_C/L_{syn}$ , gives the ratio of the  $\gamma$ -ray and synchrotron luminosities, assuming that the  $\gamma$  rays are from Compton scattering by the same jet electrons making the synchrotron emission; and
5.  $\epsilon_c = h\nu_c/m_e c^2$ , where the peak Compton frequency  $\nu_c$  is the frequency at which the  $\nu L_\nu$  Compton spectrum reaches its maximum value.

A complete SED contains additional information in the detailed features of the spectrum. In particular, the Compton component in blazars is generally a composite of the SSC and EC components, the latter of which depends on the external radiation environment. IR from thermal dust, the stellar content of the host galaxy, and hot accretion-disk radiation may all contribute to the IR – UV radiation spectrum, and must be considered when fitting data.

Within the framework we set up, the derived synchrotron/SSC/EC model parameters are:

1.  $B'$ , the comoving magnetic field, in G;
2.  $\delta_D$ , the Doppler factor;
3.  $\gamma'_{pk}$ , the peak electron Lorentz factor;
4.  $r'_b = c\delta_D t_{var}$ , the comoving radius of the emission region;
5.  $u_i$ , the external radiation field energy density; and
6.  $\epsilon_i = h\nu_i/m_e c^2$ , the dimensionless external radiation photon frequency,

with  $i$  indexing the various radiation fields in the blazar's environment. In standard modeling approaches,  $B'$ ,  $\delta_D$  and  $u_i$  are adjusted to obtain a good fit, whereas in this approach, the equipartition assumption determines  $B'$ ,  $\delta_D$ , and  $\gamma'_{pk}$ , assuming that the equipartition condition is valid, while spectral fitting implies  $u_i$ .

The dynamical crossing time associated with the Schwarzschild radius of a  $10^9 M_\odot$  black hole is  $\approx 10^4 \text{ s}$ . Here we let  $t_4 = 1$  in most of our calculations, noting that this parameter should be determined from blazar variability measurements at the time that the observing campaign took place.

The comoving magnetic field energy density  $u'_{B'} = B'^2/8\pi$ . In the standard blazar model, we can write the total comoving energy density  $u'_{tot}$  of particles, field, and radiation in the outflowing plasma blob through the expression

$$u'_{tot} = u'_{B'} + u'_{par} + u'_{ph} = u'_{B'}(1 + \zeta_{par} + \zeta_{ph}). \quad (4)$$

The subscripts refer to magnetic field ( $B'$ ), both large-scale ordered and disordered fields, including MHD waves; particles (par), divided into electronic (e) and nuclear (p/nuc) components (thus  $\zeta_{par} = \zeta_e + \zeta_{p, nuc}$ ); and photons (ph). We separately calculate the particle and field power, on the one hand, and the photon power on the other. The photon fields consist of the internal synchrotron (syn) and SSC fields, and the Compton-scattered  $\gamma$  rays.

The simplest equipartition relation is  $u'_e = \zeta_e u'_{B'}$ ,  $\zeta_e \cong 1$ , which also minimizes jet power.<sup>6</sup> We also let  $\zeta_{p, nuc} = 1$  in the following calculations, representing a jet with low baryon content. The baryonic content affects only the total power and not spectral properties; see Section 6.4.

### 3.2. Constraints and equipartition relations

One advantage of using the log-parabola function, besides having only three parameters to characterize the nonthermal electron distribution, is that in the limit  $b \rightarrow \infty$ , the electrons become monoenergetic. The solution, along with corrections related to the width of the log-parabola electron distribution, is derived in the Appendix. The  $b \rightarrow \infty$  limit is obtained by letting  $f_1 \rightarrow 1$  and  $f_2 \rightarrow 1$  in the equations below; see Table 1). The analytic results provide parameters as input for the numerical model.

<sup>6</sup> The particle energy density is 4/3rd the magnetic-field energy density at minimum jet power; see (see, e.g., Ghisellini & Celotti 2001; Finke et al. 2008). For simplicity, we let  $\zeta_e = 1$  and  $\zeta_{p, nuc} = 1$  in the calculations.

TABLE 1  
LOG-PARABOLA AND GEOMETRY CORRECTION FACTORS

$I(b)$	$\sqrt{\pi \ln 10/b}$
$f_0$	$1/3$
$f_1$	$10^{-1/4b}$
$f_2$	$10^{1/b}$
$f_3$	$\frac{f_1}{2I(b)} = \frac{10^{-1/4b}}{2\sqrt{\pi \ln 10/b}}$

A first constraint arises from simple kinematics. In a blob geometry, the comoving synchrotron energy density  $u'_{syn} = L_{syn}/4\pi r'_b{}^2 c \delta_D^4 f_0$ , where  $r'_b \cong c \delta_D t_{var}$ , so

$$L_{syn} = 4\pi t_{var}^2 c^3 \delta_D^6 u'_{syn} f_0, \quad (5)$$

where  $f_0$  is a factor of order unity,<sup>7</sup> and  $u'_{syn} \equiv \zeta_s u'_{B'}$ , relates the internal synchrotron and magnetic fields. A second constraint is the synchrotron luminosity constraint

$$L_{syn} = \frac{4}{3} c \sigma_T u'_{B'} N_{e0} \gamma_{pk}^2 \delta_D^4, \quad (6)$$

which takes this form even with log-parabola width corrections, as shown in the Appendix, Equation (B4). When the equipartition relation

$$u'_e = \frac{\mathcal{E}'_e}{V'_b} = \frac{m_e c^2 N_{e0} \gamma'_{pk}}{V'_b} f_1 = \zeta_e u'_{B'}, \quad (7)$$

with  $V'_b = 4\pi r'_b{}^3/3$  and  $f_1 \equiv 10^{-1/4b}$  (see Appendix, Equation (A6)), is substituted into the synchrotron constraint, Equation (6), and the result is equated with  $L_{syn}$  given by Equation (5), we find

$$\zeta_s = \frac{4}{9} \sigma_T u'_{B'} \frac{r'_b}{m_e c^2 f_0 f_1} \zeta_e \gamma'_{pk}. \quad (8)$$

The peak synchrotron frequency can be expressed in terms of the critical magnetic field  $B_{cr} = m_e^2 c^3 / e \hbar$  as

$$\epsilon_s = f_2 \epsilon_{pk} = f_2 \delta_D \epsilon'_{pk} = f_2 \delta_D \frac{3}{2} \frac{B'}{B_{cr}} \gamma_{pk}^2, \quad (9)$$

where  $f_2 \equiv 10^{1/b}$ , from which, with Equation (8), we derive

$$\delta_D B'^3 = \frac{3f_2}{2B_{cr} \epsilon_s} \left( \frac{18\pi m_e c f_0 f_1 \zeta_s}{\sigma_T t_{var} \zeta_e} \right)^2. \quad (10)$$

Replacing this result in eq. (5) gives

$$\begin{aligned} \delta_D &= \left( \frac{2L_{syn}^3}{3^{10} \pi^4 f_0^7 \zeta_s^7 c^{13}} \right)^{1/16} \left( \frac{\sigma_T \zeta_e}{f_1 m_e} \right)^{1/4} \left( \frac{B_{cr} \epsilon_s}{f_2 t_{var}} \right)^{1/8} \\ &\cong 17.5 L_{48}^{3/16} \frac{\zeta_e^{1/4} \nu_{14}^{1/8}}{\zeta_s^{7/16} t_4^{1/8}} \frac{1}{f_0^{7/16} f_1^{1/4} f_2^{1/8}}. \end{aligned} \quad (11)$$

Inverting Equation (9) to get an expression for  $B'$  as a function of  $\delta_D$ , and using Equation (11) for  $\delta_D$ , gives

$$B'(G) \cong \frac{5.0 \zeta_s^{13/16}}{L_{48}^{1/16} t_4^{5/8} \nu_{14}^{3/8} \zeta_e^{3/4}} f_0^{13/16} f_1^{3/4} f_2^{3/8}. \quad (12)$$

<sup>7</sup> For a spherical blob geometry,  $f_0 \cong 1/3$ . For a spherical shell geometry,  $f_0 \cong 1$  and  $\delta_D \rightarrow \Gamma$ .

Using eqs. (9), (11), and (12), we have

$$\gamma'_{pk} \cong 523 \frac{\nu_{14}^{5/8} \zeta_e^{1/4}}{L_{48}^{1/16} \zeta_s^{3/16}} t_4^{3/8} \frac{1}{f_0^{3/16} f_1^{1/4} f_2^{5/8}}. \quad (13)$$

### 3.3. EC component

In the Thomson regime, the peak frequency of the external Compton-scattered component is

$$\epsilon_T^{EC} \cong f_2 \frac{4}{3} (\delta_D \gamma'_{pk})^2 \epsilon_* \cong 2 \times 10^3 \frac{\epsilon_*}{2 \times 10^{-5}} \frac{\zeta_e}{\zeta_s^{5/4}} \frac{\nu_{14}^{3/2} t_4^{1/2} L_{48}^{1/4}}{f_0^{5/4} f_1 f_2^{1/2}}, \quad (14)$$

normalizing to the Ly  $\alpha$  energy  $\epsilon_* \cong 2 \times 10^{-5}$  for the mean photon energy in the external radiation field. The onset of the Klein-Nishina correction for external Compton scattering takes place when  $4\gamma'_{pk} \epsilon' \gtrsim 1$ . Taking  $\epsilon' \cong \delta_D \epsilon_*$ , the photon energy in the stationary frame where KN effects become important is at  $\epsilon_{C,KN} = 1/12\epsilon_*$ . For Ly $\alpha$  target photons,  $\epsilon_{Ly\alpha} = 1$ ,  $E_{C,KN} \cong 2.2$  GeV, and this could be the reason for the spectral cutoff in FSRQs and low-synchrotron peaked (LSP;  $\nu_s^{obs} < 10^{14}$  Hz) blazars (Ackermann et al. 2010; Cerruti et al. 2013). The strongest dependence of the peak frequency of the external Compton component is  $\epsilon_T^{EC} \propto \nu_{14}^{3/2}$ , so that most FSRQs with  $\nu_{14} \cong 0.1$  have  $\epsilon_T^{EC} < \epsilon_{C,KN}$ , and the combined effects of the softening electron spectrum and Klein-Nishina cross section make an apparent cutoff at  $\approx \epsilon_{C,KN}$ .

### 3.4. SSC component

The peak  $\gamma$ -ray energy in the Thomson approximation of the SSC spectrum is approximately given by

$$\begin{aligned} \epsilon_T^{SSC} &\cong f_2 \frac{4}{3} \delta_D \gamma_{pk}^2 \epsilon'_s \cong f_2 \frac{4}{3} \gamma_{pk}^2 \epsilon_s \\ &\cong \frac{9.4 \times 10^3}{f_0^{3/8} f_1^{1/2} f_2^{1/4}} \frac{\zeta_e^{1/2} t_4^{3/4} \nu_{16}^{9/4}}{\zeta_s^{3/8} L_{48}^{1/8}}, \end{aligned} \quad (15)$$

defining  $\nu_{16} = \nu_s/10^{16}$  Hz. Compared with the Thomson approximation, Klein-Nishina effects in SSC scattering are important for SSC  $\gamma$  rays with energies  $\epsilon_{KN}^{SSC} \cong (4/3) f_2 \gamma_{pk}^2 \epsilon_s \cong f_2 \gamma'_{pk} \delta_D/3$ . Thus

$$\epsilon_{KN} \cong 3050 \nu_{14}^{3/4} t_4^{1/4} L_{48}^{1/8} \frac{f_2^{1/4} \zeta_e^{1/2}}{f_0^{5/8} f_1^{1/2} \zeta_s^{5/8}}. \quad (16)$$

For a given parameter set, KN effects are important when  $\epsilon_s \gtrsim \epsilon_{s,KN} = \delta_D/4\gamma'_{pk}$ , that is, for synchrotron photons with energies greater than  $\epsilon_{s,KN}$ , where

$$\epsilon_{s,KN} \cong 8.4 \times 10^{-3} \sqrt{\frac{\sqrt{f_2 L_{48}/f_0 \zeta_s}}{f_1 \nu_{14} t_4}}, \quad (17)$$

or

$$\nu_{14,KN} \cong \frac{470}{(f_1 t_4)^{1/3}} \left( \frac{f_2 L_{48}}{f_0 \zeta_s} \right)^{1/6}. \quad (18)$$

Thus, KN effects are most important in high-synchrotron peaked (HSP;  $\nu_s^{obs} > 10^{15}$  Hz) BL Lac objects.

### 3.5. Synchrotron self-absorption

We use the  $\delta$ -function approximation to calculate synchrotron self-absorption (SSA). The SSA coefficient for a photon of frequency  $m_e c^2 \epsilon' / h$  in the fluid frame is given in this approximation by

$$\kappa_{\epsilon'} = \frac{-\pi}{36} \frac{\lambda_C r_e}{\epsilon'} \left[ \gamma'_s \frac{\partial}{\partial \gamma'_s} \left( \frac{n'_e(\gamma'_s)}{\gamma'^2_s} \right) \right], \quad \gamma'_s = \sqrt{\epsilon' / 2\epsilon_{B'}} , \quad (19)$$

(Dermer & Menon 2009, eq. (7.144), with corrections). Here  $\lambda_C = h/m_e c$  is the Compton wavelength,  $r_e = e^2/m_e c^2$  is the classical electron radius, and  $\epsilon_{B'} = B'/B_{cr}$ . Taking  $n'_e(\gamma') = N'_e(\gamma')/V'_b$ , and substituting Equation (2) for  $N'_e(\gamma')$  gives

$$\kappa_{\epsilon'} = \frac{\pi}{18} \frac{\mathcal{E}'_e}{m_e c^2 I(b) V'_b \gamma'^4_{pk}} \frac{\lambda_C r_e}{\epsilon'} (2 + b \log \hat{y}) \hat{y}^{-(4+b \log \hat{y})} , \quad (20)$$

where  $\hat{y} \equiv \sqrt{\epsilon' / 2\epsilon_{B'}} / \gamma'_{pk}$ .

The SSA opacity  $\tau_{\epsilon'} = 2\kappa_{\epsilon'} r'_b$ . The unabsorbed spectrum is multiplied by the factor  $u(\tau) = 1/2 + \exp(-\tau)/\tau - [1 - \exp(-\tau)]/\tau^2$ , with  $\tau = \tau_{\epsilon'}$ , to give the absorbed spectrum (Gould 1979).

### 3.6. Jet power

We calculate absolute jet power  $L_{jet}$  for a two-sided jet using the relation

$$L_{jet} = L_{B,par} + L_{ph} = 2\pi r_b^2 \beta \Gamma^2 c (u'_{B'} + u'_{par}) + L_{ph} \quad (21)$$

(Celotti & Fabian 1993; Celotti & Ghisellini 2008, compare Equation (4)). The absolute photon power  $L_{ph} = L_{abs,s} + L_{abs,C}$  is separately evaluated from the magnetic-field and particle power,  $L_{B,par}$ , because the photon distributions in the comoving frame can have peculiar anisotropies associated with the different angular distributions of internal and external Compton scattering (Dermer 1995). The apparent  $L_{syn}$  and absolute  $L_{abs,s}$  synchrotron and SSC fluxes are related by the expression

$$L_{abs,syn} = 8\Gamma^2 L_{syn} / 3\delta_D^4 . \quad (22)$$

For external Compton (C) emission, the relationship is

$$L_{abs,C} = 32\Gamma^4 L_C / 5\delta_D^6 \quad (23)$$

(see Appendix A in Dermer et al. 2012).

These very different behaviors are important for power requirements in jets. The kinetic power,  $L_{B',par} = (1 + \zeta_e + \zeta_{p,nuc}) \Gamma u'_B V'_b / t_{var}$ , accounts for the magnetic-field and particle energy in the jet. In our model calculations, the magnetic-field and particle power is dominated by the photon power  $L_{ph}$ , so that baryon-loading does not have a big impact on jet power requirements until  $\zeta_{p,nuc} \gg 1$ . In actual fitting to 3C 279, we find that  $L_{B,par} \approx L_{ph}$ .

## 4. NUMERICAL RESULTS

Using the derived values of  $\delta_D$ ,  $B'$ ,  $\gamma'_{pk}$ , and  $r'_b$ , along with the log-parabola description of the electron spectrum, Equation (1), we numerically calculate  $\nu L_\nu$  SEDs. The method for calculating the SEDs are presented in Finke et al. (2008) and Dermer et al. (2009). Assuming that the external radiation fields are locally isotropic, the assumed isotropic distribution of electrons in the

jet frame is transformed to the source frame through the expression  $N(\gamma, \Omega) = \delta_D^3 N'(\gamma') / 4\pi$ , so all angular dependence of the particle distribution in the stationary black-hole frame from the small spherical jet blob is in the Doppler factor (Georganopoulos et al. 2001). The spectrum of external Compton  $\gamma$  radiation is calculated assuming the head-on approximation for the Compton cross section, which applies to all but  $\sim 1/\gamma^2$  of the photons for scattering by electrons with Lorentz factor  $\gamma$ . Furthermore, the scattered photon is assumed to travel in the direction of the incident electron, which holds when  $\epsilon \ll \gamma$ . For the head-on approximation of the Compton cross section in the general case of anisotropic and isotropic external radiation fields, see eqs. (6.97) and eq. (6.113) in Dermer & Menon (2009), respectively. The isotropic case, assumed here, recovers the Jones (1968) result.

In the model calculations shown in this section, we calculate SEDs for external isotropic photon sources with  $\epsilon_* = 2 \times 10^{-5}$  characterizing the BLR (10.2 eV), and  $\epsilon_* = 5.4 \times 10^{-7}$  ( $\cong 0.3$  eV) describing radiation from a hot dust torus at 1200 K temperature. The former value is motivated by the strong Ly $\alpha$  line in blazars, specifically, 3C 454.3 (Bonnoli et al. 2011). The latter value is motivated by observations of 4C +21.35 by Malmrose et al. (2011) who, using 5 – 35  $\mu$  Spitzer, Sloan Digital Sky Survey, Two Micron All Sky Survey and Swift UVOT data, decompose the spectrum of 4C +21.35 into a non-thermal power law and a two-temperature dust model. The warm dust component has effective temperature  $T \sim 660$  K and radiates  $\approx 10^{45}$  erg s $^{-1}$ , while the hot dust component has  $T \approx 1200$  K and with luminosity  $7.9 \pm 0.2 \times 10^{45}$  erg s $^{-1}$ . Calculations of AGN emissions reprocessed by dust clouds (Nenkova et al. 2008a,b) show that the peak power of the reprocessed emission occurs at  $\approx 10\mu$  (the 10 $\mu$  silicate feature), with broad wings from  $\approx 3\mu$  to  $\sim 30\mu$ . This peak frequency corresponds to  $\epsilon_* \approx 2 \times 10^{-7}$ , or an effective blackbody temperature of  $\approx 500$  K, characteristic of warm dust.

When fitting actual blazar spectra, both IR dust and BLR photon sources contribute and have to be appropriately adjusted to give a good fit. Detailed fitting requires a range of atomic lines and multiple thermal components (Cerruti et al. 2013), but this two-line simplification illustrates the technique.

Figure 1 shows model SEDs for values characteristic of a powerful FSRQ blazar with a bolometric synchrotron luminosity  $L_s \cong 5 \times 10^{47}$  erg s $^{-1}$  and peak photon frequency  $\nu_s = 10^{13}$  Hz. Input values for this and other figures in this section are given in Table 2, and derived values are listed in Table 3. In the calculations, we use the expression

$$\Gamma = \frac{1}{2} (1 + N_\Gamma^2) \delta_D \quad (24)$$

to relate  $\Gamma$  and  $\delta_D$ , where  $N_\Gamma \equiv \Gamma\theta$ , which is valid in the limit  $\Gamma \gg 1$ ,  $\theta \ll 1$ . We model off-axis blazars with  $N_\Gamma = 1$ , and on-axis blazars with  $N_\Gamma = 0$ . The BLR is approximated by an external monochromatic radiation field with line energy  $\epsilon_* = 10.2/511000 = 2 \times 10^{-5}$ , and likewise for the IR torus with mean photon energies characteristic of 440 K and 1200 K blackbodies.

The different beaming factors of the synchrotron and SSC components on the one hand and the EC compo-

TABLE 2  
BLAZAR MODEL INPUT<sup>a</sup>

Case	$\nu L_{\nu}^{pk, syn}$ ( $10^{48}$ erg/s)	$\nu_{14}$	$t_4$	$b$	$\zeta_s$	$\zeta_*^b$	$N_{\Gamma}$
1a	0.1	0.1	1	1	1	10	1
1b							0
2a	0.01	0.1	1	1	1		1
2b							0
2c				0.5			1
2d				2			
2e			0.1	1			
2f			10				
3a	0.01	0.1	1				
3b		1					
3c		10					
4a <sup>c</sup>	0.001	1					
4b		$10^1$					
4c		$10^2$					
4d		$10^3$					
4e		$10^4$					

<sup>a</sup> Soft photon energies are  $\epsilon = 2 \times 10^{-5}$ , corresponding to Ly $\alpha$  radiation in the BLR, and  $5.4 \times 10^{-7}$ , corresponding to 1200 K dust, with  $\zeta_e = \zeta_{p, nuc} = 1$ . Blank entries in Tables are equal to first filled vertical entry above. For Cases 4a-e,  $\zeta_* \rightarrow 0$ .

<sup>b</sup>  $\zeta_* = 10$  for each of the BLR and IR dust radiation fields

<sup>c</sup> Equipartition synchrotron/SSC model without external radiation fields

TABLE 3  
BLAZAR MODEL OUTPUT

Case	$\Gamma$	$\delta_D$	$B'$ (G)	$\gamma'_{pk}$	$u_0$ (erg cm <sup>-3</sup> )	$r'_b$ ( $10^{15}$ cm)	$\log[L_{B, par}$ ( $L_{ph}$ ) (erg s <sup>-1</sup> )] <sup>a</sup>
1a	16.4	16.4	7.8	43.4	0.067	4.9	45.9(47.2)
1b	8.2				0.27		45.3(46.6)
2a	10.6	10.6	9.0	50.0	0.21	3.2	45.3(46.6)
2b	5.31				0.85		44.7(46.0)
2c	9.8	9.8	13.5	44.9	0.57	2.9	45.5(46.8)
2d	10.7	10.7	7.4	97.8	0.14	3.2	45.2(46.4)
2e	14.2	14.2	38	21	2.1	0.42	45.1(46.3)
2f	8.0	8.0	2.1	119	0.021	24	45.6(46.8)
3a	10.6	10.6	9.00	50.0	0.21	3.2	45.3(46.6)
3b	14.2	14.2	3.80	211	0.021	4.2	45.1(46.2)
3c	18.9	18.9	1.60	890	0.0021	5.7	44.8(45.8)
4a	9.2	9.2	4.37	244	–	2.8	44.4(44.4)
4b	12.3	12.3	1.84	1030		3.7	44.2(44.2)
4c	16.4	16.4	0.78	4340		4.9	43.9(43.9)
4d	21.8	21.8	0.33	1.83e4		6.5	43.7(43.7)
4e	29.1	29.1	0.14	7.71e5		8.7	43.4(43.2)

<sup>a</sup>  $L_{B, par}$  is two-sided absolute magnetic-field and particle power, and  $L_{ph}$  is photon power; see Equation (21)

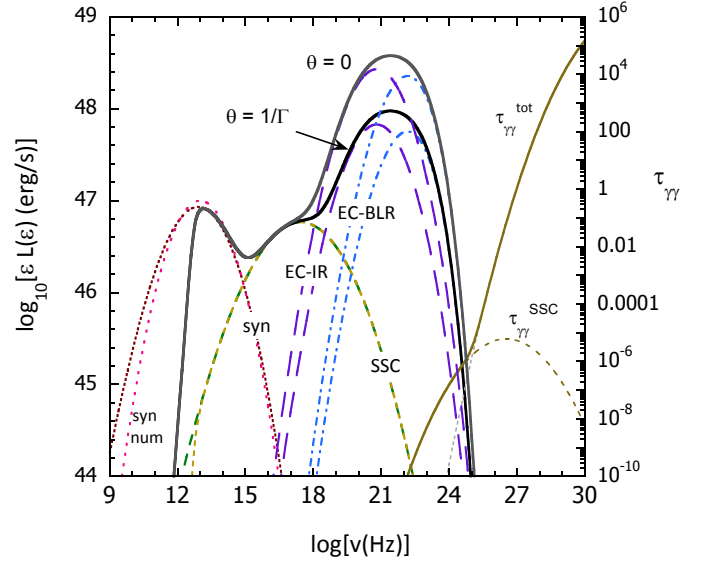


FIG. 1.— Model blazar SEDs from radio to  $\gamma$  rays implied by equipartition conditions, using synchrotron luminosities and peak frequencies characteristic of a powerful FSRQ. In this calculation,  $\zeta_* = 10$  for each of the BLR and IR components, and  $\zeta_s = 1$ . The  $\nu L_{\nu}$  peak synchrotron luminosity  $\nu L_{\nu}^{pk, syn} = 10^{47}$  erg s<sup>-1</sup>, and the bolometric synchrotron luminosity is a factor  $2\sqrt{\pi \ln 10} \cong 5.38$  larger. Jets are viewed off axis,  $\theta \cong 1/\Gamma$ , and on-axis,  $\theta = 0$ , as labeled. The BLR target photons are approximated as Ly $\alpha$  ( $\epsilon_* = 2 \times 10^{-5}$ ), and the IR radiation as monochromatic photons with energy ( $\epsilon_* = 5.38 \times 10^{-7}$ ). Separate synchrotron, SSC, and EC components are shown. Analytic expressions for the synchrotron SED (“syn num”) and  $\gamma\gamma$  opacity through the synchrotron and SSC fields ( $\tau_{\gamma\gamma}$ ) are also plotted.

nents on the other are seen when the  $\nu L_{\nu}$   $\gamma$ -ray SEDs for  $\theta = 1/\Gamma$ ,  $\delta_D = \Gamma$  is compared with the SED for  $\theta = 0$ ,  $\delta_D = 2\Gamma$  (Dermer 1995; Georganopoulos et al. 2001). In Figure 1,  $\Gamma \approx 16$  for  $\theta = 1/\Gamma$  and  $\Gamma \approx 8$  for  $\theta = 0$ , with photon energy densities  $u_0 \approx 0.067$  erg cm<sup>-3</sup> and  $u_0 = 0.27$  erg cm<sup>-3</sup> for the off- and on-axis cases, respectively. A larger external energy density is required for the on-axis jet model when all other parameters are the same, because the implied  $\Gamma$  factor is smaller. The magnetic field  $B' \cong 8$  G and  $\gamma'_{pk} \cong 43$ .

For the equipartition solution, a break is formed at  $\approx 400$  MeV – GeV energies when jet electrons scatter Ly $\alpha$ /BLR photons (Cerruti et al. 2013). If IR photons alone are scattered, the  $\nu L_{\nu}$  spectrum peaks near 10 MeV and the break is at higher energies, but below 1 GeV. If the electrons in the flaring jet are within the BLR, they scatter both IR and BLR photons, whereas when the radiating jet is found far outside the BLR, scattering of IR photons dominates. So an FSRQ with a GeV break would also be accompanied by a  $\gamma$ -ray external Compton dust feature. In contrast, flares occurring far outside the BLR would make a blazar SED peaked at MeV energies, as seen in some blazars with low Compton peak frequencies, e.g., CTA 102 and PKS 0528+134 (McNaron-Brown et al. 1995).

The value  $\zeta_s = 1$  in Figure 1, and the bolometric SSC luminosity is equal to the synchrotron luminosity  $L_{syn}$  considering that the SSC SED has a larger width (or smaller effective value of  $b$ ) than the synchrotron SED’s

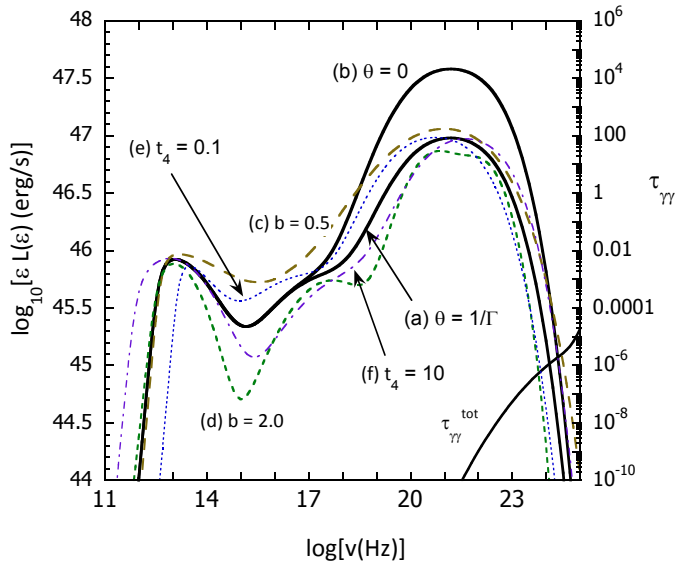


FIG. 2.— Similar to Fig. 1, except that  $\nu L_{\nu}^{pk, syn} = 10^{46}$  erg  $s^{-1}$ . Effects of varying  $b$  and  $t_4$  on the SED are shown as labeled. Opacity is shown for case (a).

width. Also shown here is a  $\delta$ -function expression for the synchrotron luminosity spectrum  $\epsilon L_{syn}(\epsilon) = \nu x^{1-\hat{b} \ln x}$ , derived in the Appendix, Equation (B1). Here  $x = \sqrt{\epsilon/\epsilon_s}$  and  $\nu = c\sigma_T B'^2 \delta_D^4 \gamma'_{pk} K/12\pi$ ; see Eq. (3). The actual peak photon energy  $\epsilon_s$  of the luminosity spectrum is simply  $\epsilon_s = \epsilon_{pk} 10^{1/b}$ .

The SSC spectrum, using either the optically thin or the self-absorbed target synchrotron photon fields, is shown for comparison in Fig. 1. The effects of self-absorption on the SSC spectrum are negligible. Because of the stronger Klein-Nishina effects for the scattered BLR photons, the Compton-scattered Ly $\alpha$  component has a smaller apparent luminosity than that of the dust component. The absolute jet luminosities for these cases almost reach the Eddington luminosity for a  $10^9 M_{\odot}$  black hole when  $\theta = 1/\Gamma$ , but are significantly less if viewed on-axis. The internal  $\gamma\gamma$  opacity of a photon through the assumed isotropic synchrotron and SSC radiation fields are calculated following the results of Appendix C. Internal absorption does not play an important role in these calculations. Opacity of  $\gamma$  rays from external BLR and IR photons depend on the location of the  $\gamma$ -ray source and characteristic size of the target photon field (Dermer et al. 2012; Tavecchio & Ghisellini 2012). Absorption on H Ly  $\alpha$  and other BLR photons can be important above  $\gtrsim 25$  GeV, and at even lower energies on high-ionization lines such as He II Ly  $\alpha$  if  $\gamma$ -ray production takes place deep within the BLR (Poutanen & Stern 2010; Stern & Poutanen 2011). When  $\gamma\gamma$  opacity is important, cascade emission may contribute to the SED. We neglect opacity of VHE  $\gamma$  rays through the BLR and IR torus in the calculations, but return to this issue in Section 6.6.

Figure 2 shows a calculation similar to Figure 1, but with an order-of-magnitude smaller apparent synchrotron luminosity, now with  $\nu L_{\nu}^{pk, syn} = 10^{46}$  erg  $s^{-1}$ , but with the same synchrotron peak frequency. The val-

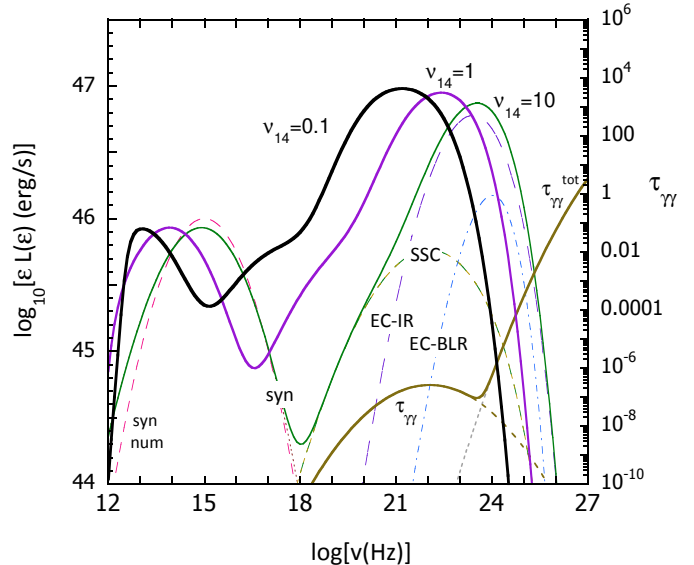


FIG. 3.— Equipartition models with input parameters characteristic of ISP blazars like 3C 66A and W Comae. Here  $\nu L_{\nu}^{pk, syn} = 10^{46}$  erg  $s^{-1}$ ,  $\zeta_s = 1$ ,  $\zeta_* = 10$  for the IR and BLR radiation fields, and synchrotron peak frequencies  $\nu_{14} = 0.1, 1$ , and 10 are considered. Separate spectral components and the  $\tau_{\gamma\gamma}$  opacity curve are shown for the  $\nu_{14} = 10$  case.

ues of  $\Gamma$  for standard off-axis and on-axis cases (a) and (b) become smaller than in the comparable cases shown in Figure 1, but the energy densities of the external radiation fields must then become larger in order to produce the same Compton dominance (Table 3). The absolute jet powers become smaller, though not decreasing as rapidly as  $L_{abs} \propto L_s^{-1}$ . Again, the equipartition solution ( $\zeta_e = 1$ ) with  $t_4 = 1$  gives a breaking GeV spectrum from target Ly $\alpha$  photons, while the upscattered IR photons peak at  $\sim 1 - 10$  MeV in a  $\nu F_{\nu}$  SED, breaking at  $\gtrsim 10 - 100$  MeV.

For comparison, we consider how different values of  $b = 0.5, 1.0$ , and 2.0, and  $t_4 = 0.1$  and 10 affect the SED and values of derived quantities in the equipartition model. Varying  $b$  changes the UV and hard X-ray fluxes by larger factors than the GeV  $\gamma$ -ray flux. The self-absorption frequency is strongly dependent on  $t_4$ , which determines the emission region size. See Tables 2 and 3 for quantitative values and results.

Figure 3 shows calculations for parameters characteristic of Intermediate Synchrotron Peaked (ISP) blazars, defined (Abdo et al. 2010c) as blazars with observed peak synchrotron frequencies in the range  $10^{14}$  Hz  $< \nu_s^{obs} < 10^{15}$  Hz. The synchrotron and external Compton parameters are kept as before, with  $\zeta_s = 1$  and  $\zeta_* = 10$  for each of the two external radiation fields, while varying the value of  $\nu_{14}$  from 0.1 to 10. The different SEDs for target IR and Ly $\alpha$  radiation fields are shown by the thin and thick curves for the  $\nu_{14} = 10$  case. As can be seen from Tables 2 and 3, larger values of  $\nu_s$  imply larger values of  $\Gamma$  and  $\gamma'_{pk}$ , the combined effect of which greatly increases Compton-scatter power in the Thomson regime (for a fixed external field energy density), while at the same time emission at GeV energies and higher becomes strongly inhibited by Klein-Nishina effects when



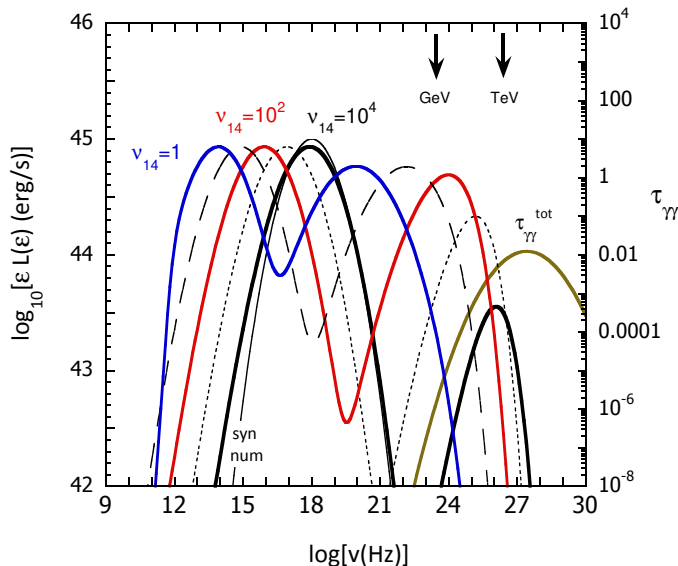


FIG. 4.— Equipartition SSC models characteristic of high-synchrotron peaked BL Lac objects. The model shows results for  $\nu L_{\nu}^{pk, syn} = 10^{45} \text{ erg s}^{-1}$ ,  $\zeta_s = 1$ , and  $\log \nu_{14} = 0, 1, 2, 3, 4$ , corresponding to curves (a) through (e), respectively (see Table 2). The analytic synchrotron solution, Equation (B1), is also shown for case (e).

scattering external UV photons, so that SEDs could become increasingly dominated by  $\gamma$  rays produced from target IR torus photons in the larger  $\nu_{14}$  cases. For these ISP-type parameters, structure may be found in the GeV regime due to the competition between SSC and Compton-scattered Ly $\alpha$  photons under conditions where the Compton dominance is not too large. An inverted spectrum can also be formed at X-ray energies where the  $\gamma$  rays from Compton-scattered dust radiation starts to dominate the SSC emission. Such a feature may be present in the SED of 3C 66A (Abdo et al. 2011d), but will require better data and fitting to establish.

Figure 4 shows equipartition models for blazars with characteristics similar to those of HSP BL Lac objects. Comparison of models 4(c) – 4(e) with the SEDs of Mrk 421 and Mrk 501 from multiwavelength campaigns of Abdo et al. (2011b) and Abdo et al. (2011c), respectively, suggest that these TeV BL Lac objects can be well fit with our equipartition model with different values of  $b$ , but quantitative statements will require a dedicated study.

For this parameter set, we also calculated the energy density of Ly $\alpha$  radiation needed to make a significant contribution to the  $\gamma$ -ray fluxes. When  $u_{Ly\alpha} \gtrsim 10^{-4} \text{ erg cm}^{-3}$ , the emission would make an EC component with  $\nu L_{\nu} \gtrsim 10^{41.5} \text{ erg s}^{-1}$ , just barely visible in the  $\nu L_{\nu}$  spectrum. The Ly $\alpha$  energy densities in Mrk 421 and Mrk 501 are, however, far below this level. Stocke et al. (2011) report Ly $\alpha$  luminosities of  $2.4$  and  $5.2 \times 10^{40} \text{ erg s}^{-1}$  for Mrk 421 and Mrk 501, respectively. The total jet power is  $\approx 10^{44} \text{ erg s}^{-1}$  for the models in Fig. 4, and the accretion-disk luminosity  $L_d$  should be greater than this if most of the jet energy comes from mass accretion (black-hole rotational energy could supply a comparable amount). Even for a BLR as small as  $0.01 \text{ pc}$ , the Ly $\alpha$  energy density  $u_{Ly\alpha} \approx 10^{40} L_{40} / 4\pi R_{0.01pc}^2 \approx 3 \times 10^{-5}$

$\text{erg cm}^{-3}$ , far smaller than what is necessary to make the EC  $\gamma$ -ray flux brighter than the SSC flux.

The low Ly $\alpha$  luminosities of Mrk 421, Mrk 501, and also PKS 2005-489 and PKS 2155-304 (Stocke et al. 2011), two other HSP BL Lac objects, are in accord with the thinking that TeV blazars have a very tenuous BLR environment, for example, by their formation history (Böttcher & Dermer 2002). By contrast, FSRQs can have very large Ly $\alpha$  luminosities. In the case of 3C 454.3, it reached  $\approx (2 - 4) \times 10^{45} \text{ erg s}^{-1}$  (Bonnoli et al. 2011).

## 5. MODELING THE SEDS OF 3C 279

Hayashida et al. (2012) have organized 3C 279 campaigns around Fermi-LAT with great results. The data in Figures 5 and 6 show SEDs from quasi-simultaneous observing campaigns for four periods of Fermi-LAT observation, namely Epochs A (MJD 54682 - 54729; 4 Aug 2008 – 19 Sept 2008), B (MJD 54789 - 54809; 19 Nov 2008 – 9 Dec 2008), C (MJD 54827-54877; 27 Dec 2008 – 15 Feb 2009), and D (MJD 54880-54885; 18 Feb 2009 – 23 Feb 2009). The SEDs comprise X-ray data from Suzaku,<sup>8</sup> Swift XRT, XMM Newton and RXTE, optical/UV data from Kanata, GROND and Swift UVOT (170-650 nm), IR data from Spitzer, and radio data from CARMA and OVRO. For comparison, also shown in the lower panel of Fig. 6 are data from the non-simultaneous VHE MAGIC detection of flare from 3C 279 flare in 2007 January (MAGIC Collaboration 2008; Aleksić et al. 2011; Şentürk et al. 2013).

### 5.1. Accretion disk and thermal dust radiation spectrum

A complete model of the blazar SED requires, for consistency, the emission spectrum from the accretion disk and from the dust. The accretion-disk spectral luminosity is assumed to be described by a Shakura-Sunyaev disk spectrum given by

$$\epsilon L_{disk}(\epsilon) = 1.12 L_{disk} \left( \frac{\epsilon}{\epsilon_{max}} \right)^{4/3} \exp(-\epsilon/\epsilon_{max}), \quad (25)$$

normalized such that  $\int_0^\infty d\epsilon L(\epsilon) = L_{disk}$  ( $1.12 \cong 1/\Gamma(4/3)$ ). The  $\nu F_\nu$  spectrum of the accretion-disk is therefore  $f_{obs}^{ad} = \epsilon L_{disk}(\epsilon) / 4\pi d_L^2$ , where  $\epsilon = (1+z)\epsilon^{obs}$  and  $d_L$  is the luminosity distance. The value of  $\epsilon_{max}$  depends on the spin of the black hole and relative Eddington luminosity, but for simplicity we let  $\epsilon_{max} = 10 \text{ eV}$ , typical of the characteristic temperature of the UV bump in Seyfert galaxies.

The spectral luminosity of the IR dust component is approximated by a thermal distribution normalized to the IR luminosity  $L_{IR}$ . Thus

$$\epsilon L_{IR}(\epsilon) = \frac{15 L_{IR}}{\pi^4} \frac{(\epsilon/\Theta)^4}{\exp(\epsilon/\Theta) - 1}, \quad (26)$$

with corresponding  $\nu F_\nu$  spectrum  $f_{obs}^{IR} = \epsilon L_{IR}(\epsilon) / 4\pi d_L^2$ . Letting  $\Theta = k_B T / m_e c^2 = 2 \times 10^{-7}$  corresponds to  $T = 1200 \text{ K}$ , but note carefully that the mean photon energy used in the monochromatic approximation is a factor  $\Gamma(4)\zeta(4)/\Gamma(3)\zeta(3) \cong 2.70$  larger than  $\Theta$ . The IR luminosity spectrum and components for the warm dust

<sup>8</sup> *Suzaku* consists of the XIS (0.3-12 keV), HXD/PIN (10-700 keV), and HXD/GSO (40-600 keV).



TABLE 4  
BLAZAR INPUT PARAMETERS FOR 3C 279<sup>a</sup>

Epoch	$\nu L_{\nu}^{pk, syn}$ ( $10^{48}$ erg s <sup>-1</sup> )	$\nu_{14}$	$b$	$\zeta_s$	$\zeta_{IR}$	$\zeta_{BLR}$	$L_{disk}$ ( $10^{46}$ erg s <sup>-1</sup> )
Aw <sup>b</sup>	0.023	0.05	0.8	0.15	2.5	7	0.55
Ah <sup>c</sup>					6	5	
Bw	0.043	0.1	0.6	0.11	2.5	18	0.5
Bh				0.1	8	12	0.55
Cw	0.06	0.2	1	0.15	4	5	0.2
Ch		0.3	1.3	0.2			
Ct5 <sup>a</sup>				0.28	8	3	
Dw					7	16	
Dh					16	5	0.5

<sup>a</sup> $t_4 = \zeta_e = \zeta_{p, nuc} = N_{\Gamma} = 1$ , except for Ct5, where  $t_4 = 10$

<sup>b</sup>w: Warm dust solution:  $\epsilon_{BLR} = 2 \times 10^{-5}$ ,  $T \cong 440$  K

<sup>c</sup>h: Hot dust solution:  $\epsilon_{BLR} = 5.4 \times 10^{-5}$ ,  $T \cong 1200$  K

TABLE 5  
MODEL OUTPUT VALUES FOR 3C 279

Epoch	$\Gamma, \delta_D$	$B'$ (G)	$\gamma'_{pk}$	$u_{IR}$ ( $10^{-3}$ erg cm <sup>-3</sup> )/ $T_{min}$ (K) <sup>a</sup>	$u_{Ly\alpha}$ ( $10^{-3}$ erg cm <sup>-3</sup> )	$\log[L_{B, par}$ ( $L_{ph}$ ) (erg s <sup>-1</sup> )]
Aw	25.7	2.6	31.6	0.77/560	2.16	45.8(45.8)
Ah				1.85/690	1.5	45.8(45.9)
Bw	35.0	1.8	28.7	0.19/400	1.4	46.0(46.1)
Bh	36.5	1.7	29	0.49/500	0.74	46.0(46.1)
Cw	37.2	1.3	99	0.15/370	0.19	45.8(45.8)
Ch	34.8		164	0.17/390	0.21	45.7(45.8)
Ct5	22.5	0.41	364	0.03/250	0.08	45.9(46.1)
Dw				0.30/440	0.68	45.7(46.1)
Dh				0.68/550	0.21	45.7(46.2)

<sup>a</sup>Minimum blackbody temperature to exceed  $u_{IR}$

model shown in Figs. 5 and 6 correspond to a dust temperature  $T \cong 440$  K, a factor 2.7 less than 1200 K, so that  $2.70 \times \Theta = 2 \times 10^{-7}$ , as well as the 1200 K dust.

A dust covering factor of 20% is assumed, so that  $L_{IR} = 0.2L_{disk}$ . The energy density of the IR radiation is limited by the energy density of a blackbody, namely

$$u_{bb}(\text{erg cm}^{-3})(T) = 9.36 \times 10^{24} \Theta^4 \\ \cong 3 \times 10^{-4} \left(\frac{T}{440 \text{ K}}\right)^4 \cong 0.016 \left(\frac{T}{1200 \text{ K}}\right)^4. \quad (27)$$

Thus the energy density at most reaches  $\approx 10^{-3}$  erg cm<sup>-3</sup> for warm dust, and  $\approx 0.02$  erg cm<sup>-3</sup> for hot dust.

### 5.2. Fits to Epochs A-D of 3C 279

Figures 5 and 6 show fits to 3C 279 from our equipartition model. The values of  $\nu L_{\nu}^{pk, syn}$  and  $\nu_s$  are input, and  $\zeta_s$  and the external radiation field parameters are varied in order to fit the data. The assumed value  $t_{var} = 10^4$  s then constrains the system to give  $\delta_D$ ,  $B'$  and  $r'_b$  through the equipartition equations, Equations (11), (12), and (13), respectively.

With the goal of limiting the number of parameters, we take  $t_4 = \zeta_e = \zeta_{p, nuc} = N_{\Gamma} = 1$ , and vary  $\zeta_s$ ,  $\zeta_{BLR}$  and  $\zeta_{IR}$ , which normalize the synchrotron, external BLR

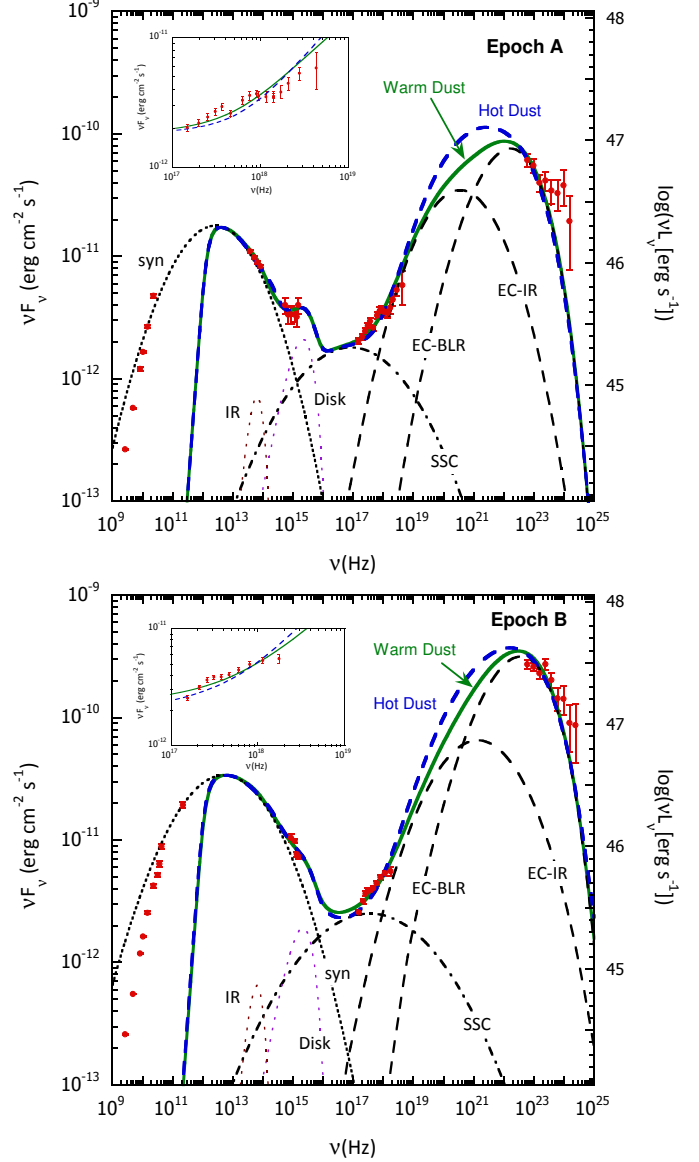


FIG. 5.— Equipartition blazar model fits to the SEDs of 3C 279 (Hayashida et al. 2012) for Epochs A (upper panel) and B (lower panel), with input parameters given in Table 4 and implied properties from the model in Table 5. Two spectral fits corresponding to warm-dust and hot-dust IR radiation fields are considered. Separate components are shown, with the EC-IR and EC-BLR components shown for the warm-dust solution. Insets show detail of fits at X-ray energies.

and IR radiation-field energy densities, respectively, until a reasonable fit to the broadband data is achieved. In fact,  $t_{var}$  can be measured, as can  $N_{\Gamma}$  if the angle to the jet axis can be determined, and such values should be used when available. The value  $\zeta_{p, nuc}$  only affects the jet power, not the spectrum, as is proved from an examination of Equations (4), (21), and (11) – (13). We keep  $\zeta_e$  equal to unity in this study, this condition taken to define equipartition.

In the fitting, there is freedom to assign the accretion-disk temperature and luminosity, and therefore the IR dust luminosity for the assumed 20% covering factor.

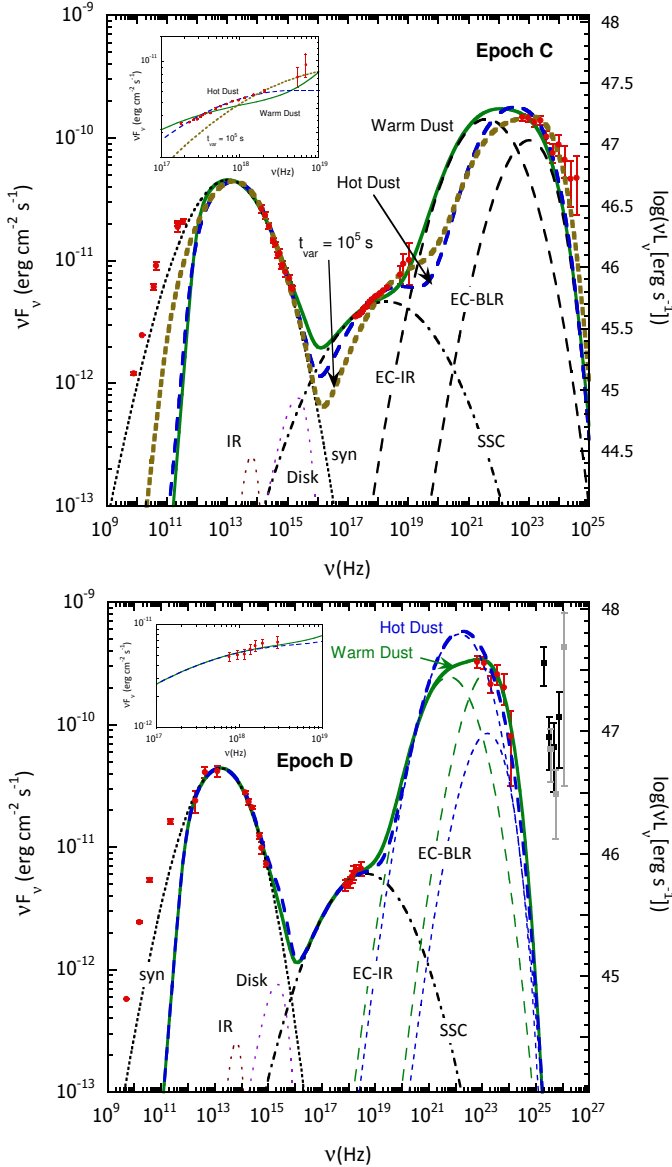


FIG. 6.— Equipartition blazar model fits to the SEDs of 3C 279 (Hayashida et al. 2012) for Epochs C (upper panel) and D (lower panel), with spectral components and inset graphs as described in Fig. 5. The upper panel shows a warm dust, hot dust, and long variability time,  $t_{var} = 10^5$  s, solution. The lower panel for the Epoch D fit shows both warm-dust and hot-dust Compton scattering components. Non-simultaneous VHE MAGIC data for 3C 279 are shown in the lower panel for comparison with the Epoch D *Fermi*-LAT  $\gamma$ -ray data.

Moreover, the accretion-disk emission can be important for fitting structure in the optical wavelength range, but in other cases gives only an upper limit to disk luminosity  $L_{disk}$ .

The results of fitting the 3C 279 data for Epochs A-D are shown in Figures 5 and 6 and listed in Tables 4 and 5. The spectral components and total spectra are shown in these figures for the case of a warm dust IR field ( $\epsilon_{IR} = 2 \times 10^{-7}$ ). A second fit with a hot-dust ( $\epsilon_{IR} = 5.4 \times 10^{-7}$ ) photon field is also shown for each of the four epochs (heavy dashed curves). The differ-

ent components, as labeled, are the unabsorbed and self-absorbed nonthermal synchrotron spectra, the IR dust self field, the Shakura-Sunyaev accretion-disk field (big blue bump), the SSC radiation, EC  $\gamma$  rays from jet electrons scattering either IR photons radiated by dust (EC-IR) or Ly $\alpha$  radiation (EC-BLR). Except at the highest  $\gamma$ -ray energies, reasonable fits with either warm and hot dust seem to be found.

Given the equipartition assumption, spectral fitting implies the energy densities of the external radiation field, given in Table 5. There we also see the minimum blackbody temperature that makes a radiation field with energy density as implied by the spectral fits. We conclude that the warm-dust models are narrowly allowed, when one considers that if only 20% of the accretion-disk radiation is re-radiated as dust, then the dust temperature has to be a factor  $\sim 5^{1/4} \sim 1.5$  larger than calculated in Table 5. The covering factor for warm dust could also be somewhat larger than  $> 20\%$ .

The significance of the implied energy densities and jet parameters are discussed in the next section. As just remarked, the fit is not satisfactory at the highest *Fermi*-LAT energies. Indeed, as shown in the bottom panel of Fig. 6, the equipartition model has no hope of fitting the MAGIC VHE data. We discuss this further below. The insets show the quality of the spectral-model fits to the X-ray data. There is a suggestion of a component peaking at  $\sim 5$  keV, but whether this could be related to the SSC component or hot plasma surrounding the supermassive black holes is unclear.

## 6. DISCUSSION

By equipartition we mean that in the fluid frame of the jet, the nonthermal electron and positron energy density is equal to the magnetic-field energy density. A system in equipartition is close to the minimum power solution, and for that reason important to study. Ideally, by choosing a suitable functional form for the electron spectrum, and measuring variability time  $t_{var}$ , the number of free parameters is sufficiently constrained that fits to data determine model parameters, including the energy densities of the surrounding radiation fields for external Compton scattering.

Hayashida et al. (2012), analyzing multiwavelength data of 3C 279, find a number of interesting results relevant here. For example, a delay by about 10 days in the optical emission compared to the  $\gamma$  rays is found from cross-correlation studies. Complex structure is observed at near- and far-IR frequencies, and an inverted spectrum is seen near  $3 \times 10^{12}$  Hz from the radio/IR data in Epoch D, with a smoothly curving synchrotron spectrum through the synchrotron  $\nu F_\nu$  peak. The extension of the synchrotron spectrum from radio/IR into optical/UV frequencies indicates a hardening in Epochs A and possibly B, as well as Epochs F and H.

Quasi-thermal radiations from the accretion disk could make the excess optical emission and apparent synchrotron hardenings. In the modeling, Shakura-Sunyaev accretion-disk emissions were used to fit the optical spectra in Epochs A and B (Figure 5). This nuclear blue-bump radiation must exist in order to illuminate the BLR (Sikora et al. 1994), and provides a powerful photon source for Compton scattering (Dermer & Schlickeiser 1993) by nonthermal electrons in the inner jet, within

the BLR.<sup>9</sup> Joint IUE/ASCA observations of 3C 279 during a low  $\gamma$ -ray state (Pian et al. 1999) found excess optical/UV radiation consistent with an accretion-disk spectrum, with disk luminosity  $L_d \approx 2 \times 10^{45}$  erg s<sup>-1</sup> and temperature reaching 20,000 K. We use  $L_d \approx (2 - 5) \times 10^{45}$  erg s<sup>-1</sup> in the equipartition model for 3C 279 (Table 4).

Because of synchrotron self-absorption, radio emission longward of  $300\mu$  ( $\approx 10^{12}$  Hz) is strongly self-absorbed in the one-zone model used here to explain blazar radiations. Long-wavelength radio emission therefore must originate from a larger volume surrounding the jet. A change in spectral and variability properties at sub-mm and longer wavelengths would be expected at the transition from optically thick to optically thin regimes. An interesting study is the dependence of the SSA frequency on model parameters, following Equation (20).

Our fits to the multi-epoch data of 3C 279, found in Figs. 5 and 6 and Tables 4 and 5, imply  $\Gamma \approx \delta_D \approx 25 - 37$  and  $B' \approx$  few G, assuming  $\theta = 1/\Gamma$  and  $t_4 = 1$ . These values can be compared with parameters used in modeling of earlier 3C 279 data by Błażejowski et al. (2000)<sup>10</sup> and Hartman et al. (2001)<sup>11</sup> when fitting to multiwavelength data associated with earlier EGRET campaigns, where reasonable fits were obtained by choosing values of  $\Gamma$  and  $B'$ . The parameters we deduce are, however, quite different from the values used to fit the same data sets in the paper by Hayashida et al. (2012). For an observing angle of  $\sim 2^\circ$  and a  $3 - 4^\circ$  opening angle jet (Jorstad et al. 2004, 2005), they chose  $B' \approx 0.15$  G and  $\Gamma \approx 15 - 20$  to fit the data, which requires large characteristic electron Lorentz factors that allows IR photons to be scattered to GeV energies. The main difference is the long assumed variability time scale in the modeling of Hayashida et al. (2012), namely  $t_{var} \sim 15$  d. The trend to such long timescales appears consistent with what we find in Fig. 6, Epoch C, when we relax the variability time to  $t_5 = 1$  (i.e.,  $t_{var} \approx 1$  d in run Ct5), so that longer timescales of variability make scattering to higher  $\gamma$ -ray energies more feasible. The relevant question then is, what value of  $t_{var}$  should be used in the various epochs?

### 6.1. Location of $\gamma$ -ray production site and variability

For only a few blazars does the *Fermi* LAT have sensitivity to probe to a few hour time scale during major outbursts, namely 3C 454.3 (Abdo et al. 2011a), PKS 1222+216 (Tanaka et al. 2011), PKS 1510-089 (Saito et al. 2013; Brown 2013), and 3C 273 (see also Foschini et al. 2011; Nalewajko 2013). Detection of much more rapid variability, as short as  $\approx 5$  min in PKS 2155-304 (Aharonian et al. 2007), and a few minutes in in

<sup>9</sup> The transition radius from the near field to far field, beyond which the accretion disk can be treated as a point source, is at  $r_{NF \rightarrow FF} \approx 0.5M_9(\Gamma/10)^4$  pc, and the transition from the dominance of accretion-disk to scattered radiation is at  $r_{NF \rightarrow sc} \approx 0.01M_9^{1/3}[r_{BLR}/(0.1 \text{ pc})]^{2/3}/(\tau/0.1)^{1/3}$  pc (Dermer & Schlickeiser 2002). Except in the inner jet, or for blazars lacking a BLR, the dominant target radiation field is the BLR or, farther out, the IR torus field (Sikora et al. 2009).

<sup>10</sup>  $B' = 0.81$  G,  $\Gamma = 20$ ,  $\theta = 1/\Gamma = 2.86^\circ$ ,  $\gamma_{br} = 150$ , with  $t_{var} \approx 20$  d.

<sup>11</sup>  $B' = 1.5$  G,  $\Gamma = 5 - 15$ , corresponding to  $t_{var} \approx 2 - 6$  d variability timescales; observing angle  $\theta = 2^\circ$  from Lähteenmäki & Valtaoja (1999).

Mrk 501 (Albert et al. 2007) and Mrk 421 (Fortson et al. 2012), could be peculiar to the TeV BL Lac objects, but 4C +21.35 has varied at 70 GeV – 400 GeV energies on timescales as short as 30 minutes. By comparison, significant MAGIC VHE detections of 3C 279 took place on two successive days, 22 and 23 February 2006 (MAGIC Collaboration 2008), after which it was also detected during a flare on 16 Jan 2007 (Aleksić et al. 2011). The VHE fluxes for the two days in 2006 were each significant, and differed by  $> 2\sigma$ , indicating day-scale variability.

The observing epochs we examine have durations of 6 days (Epoch D), 3 weeks (Epoch B), and 6 weeks (Epochs A and C). The derived energy densities of the target radiation fields for Epochs A – D of 3C 279 are  $u_{IR} \approx (0.1 - 1) \times 10^{-3}$  erg cm<sup>-3</sup> for the IR field and  $u_{Ly\alpha} \approx (0.2 - 2) \times 10^{-3}$  erg cm<sup>-3</sup> for the Ly $\alpha$  field, except for the third case in Epoch C where  $t_{var} = 10^5$  s and the implied external radiation-field energy densities are much lower. Close inspection of the light curves from radio through  $\gamma$  rays in Hayashida et al. (2012) indicates variability on a timescale as short as a fraction of a day to a few days, making the  $t_4 \approx 1 - 10$  regime most relevant for spectral fitting. A better fit to the  $\gamma$ -ray data and a worse fit to the X-ray data is found with a longer variability time.

The total external-field energy densities vary by about an order of magnitude, from  $\approx (0.4 - 3) \times 10^{-3}$  erg cm<sup>-3</sup>, for  $t_{var} \approx 10^4$  s. We can use our results to define minimum radii for  $\gamma$ -ray production, using the expression

$$u_{BLR} = \frac{\tau L_{disk}}{4\pi r_{BLR}^2 c [1 + (r/r_{BLR})^{\beta_{BLR}}]} \approx \frac{0.3\tau}{(1 + \rho^3)} \frac{\text{erg}}{\text{cm}^3} \quad (28)$$

(Sikora et al. 2009; Hayashida et al. 2012) and assuming the simple scaling relation (Ghisellini & Tavecchio 2008)

$$r_{BLR} \approx 0.1 \sqrt{\frac{L_{disk}}{10^{46} \text{ erg s}^{-1}}} \text{ pc} \quad (29)$$

between the characteristic BLR radius,  $r_{BLR}$ , and accretion-disk luminosity  $L_{disk}$ . If a fraction  $\tau \approx 0.1$  of the radiation is scattered or reprocessed into line radiation, we find that the  $\gamma$ -ray emission site takes place at  $\rho = r/r_{BLR} \sim 2 - 10$ , that is,  $\sim 0.1 - 0.5$  pc from the black hole.

Within the colliding-shell paradigm for blazars (e.g., Spada et al. 2001; Böttcher & Dermer 2010; Mimica & Aloy 2012), the collision radius  $R_{coll} \lesssim 2\Gamma^2 c t_{var} \sim 0.2(\Gamma/30)^2 t_4$  pc, which is consistent with a location at the edge of the BLR (Eq. (29)). In Epoch A, when the derived  $\Gamma$  is smallest (see Table 3), so  $R_{coll} \lesssim 0.1(\Gamma/26)^2 t_4$  pc, the probable location of the emission region is deepest within the BLR and IR torus, and the implied energy densities are largest at this epoch. Given the uncertainty on  $t_4$ , the colliding-shell radius is also on the  $\sim 0.1 - 0.5$  pc size scale of the IR dust emission where  $u_{IR}$  might change significantly, depending on the geometry of the IR torus. The scatter in IR energy density also reflects the range of model uncertainty.<sup>12</sup>

<sup>12</sup> The data gap in the 0.1 – 100 MeV range reflects sensitivity limitations of MeV telescopes. INTEGRAL observations of 3C 279 were made by Collmar et al. (2010), but unfortunately at the time when SPI was being annealed.

From Nenkova et al. (2008a,b), the inner radius due to dust sublimation is

$$R_d \simeq 0.4 \sqrt{L_{45}} \left( \frac{T_{sub}}{1500 \text{ K}} \right)^{-2.6} \text{ pc}, \quad (30)$$

where the bolometric AGN luminosity is  $10^{45} \text{ erg s}^{-1}$ , and  $T_{sub}$  is the dust sublimation temperature. Malmrose et al. (2011) argue for dust sublimation radii of  $1 - 2 \text{ pc}$ . The IR zone might not be much larger than the BLR, however, as would naturally follow if the torus and BLR clouds are the same accretion flow found at different distances from the nuclear continuum, with properties defined by whether the accreting material was inside or outside the dust-sublimation radius (Nenkova et al. 2008b).

### 6.2. Jet power calculations

The absolute two-sided jet power  $L_{jet} (\text{erg s}^{-1})$  is given by Equation (21), in terms of magnetic-field/particle power  $L_{B,par}$  and photon power  $L_{ph}$ , as reported in Table 5 for the four epochs of 3C 279, assuming  $\zeta_{p,nuc} = 1$ . Emission-line studies using  $H\beta$  line width (Gu et al. 2001) and broad line luminosity (Woo & Urry 2002) implies that 3C 279 harbors a black hole with mass  $(3 - 8) \times 10^8 M_\odot$ . The implied Eddington luminosity is therefore in the range  $(4 - 10) \times 10^{46} \text{ erg s}^{-1}$ . All our solutions have total powers below  $\approx 2 \times 10^{46} \text{ erg s}^{-1}$ , well below the Eddington luminosity, but a factor of a few higher than the accretion-disk luminosity. We find that baryon-loading factors  $\zeta_{p,nuc} \lesssim 20$  are compatible with an Eddington-limited system. The photon power is about equal to the combined magnetic-field and particle power in the jets of 3C 279; see Table 5.

The apparent isotropic bolometric  $\gamma$ -ray luminosity exceeds  $\approx 10^{48} \text{ erg s}^{-1}$  in Epoch B, whereas the total jet power is  $\lesssim 2 \times 10^{46} \text{ erg s}^{-1}$  (for  $\zeta_{p,nuc} = 1$ ). If the jet opening angle  $\theta \approx 1/\Gamma$ , then the difference between the absolute and apparent powers would be proportional to the beaming factor  $f_b$ , with  $f_b \lesssim 0.1\%$  for  $\Gamma \approx 30$ . The reduction in power is by only  $2\%$  rather than  $0.1\%$ , which shows that in relativistic nonthermal synchrotron jet models, it can be naive to use a simple beaming factor to relate the apparent isotropic and absolute powers.

### 6.3. Leptonic models for $\gamma$ -ray emission from 3C 279

The equipartition leptonic model, as presented in Figures 5 and 6, simulates reasonably well the measured SEDs of 3C 279, though the model underproduces multi-GeV  $\gamma$ -ray fluxes. A better BLR model including the line structure does not change the shape enough to explain the discrepancy (Cerruti et al. 2013). It is interesting to consider how the discrepancy can be corrected in a leptonic model. One possibility is a hardening in the electron spectrum compared to the monotonic softening in the log-parabola function. This could help explain the optical/UV hardening at the same time as enhancing fluxes at GeV energies, and could work for Epochs A and B, but not for Epoch C, where there is no evidence for hardening at optical/UV energies. Increasing the variability time as in run Ct5 allows the leptonic model to fit the  $\gamma$  rays, but the X-rays now require an additional component to compensate at soft X-ray energies. Corrections to the X-ray spectrum could involve complicating

factors, e.g., absorption, or addition of emission from a hot plasma surrounding the nucleus.

This leptonic model is therefore not entirely satisfactory, and faces another challenge when trying to explain VHE emission detected from 3C 279. Modeling by Böttcher et al. (2009) showed that leptonic models for the MAGIC data required leptonic models well out equipartition that give bad fits to the X-rays. Nevertheless, leptonic models have considerable success in fitting the broadband SED of 3C 279 in most states, so the basic blazar model may only need extended.

In the modeling performed in the Hayashida et al. (2012) paper, a conventional blazar model is used, much as described here except with a doubly broken power law to describe the electron distribution. By using a long,  $\approx 2$  week variability time, a smaller fluid magnetic field,  $B' \approx 0.15 \text{ G}$ , and smaller bulk Lorentz factors,  $\Gamma \approx 15 - 20$ , can be used, though the characteristic electron Lorentz factors must be larger. This permits IR photons to be scattered to higher energies before the Klein-Nishina suppression sets in. Except for Epoch A, where a broken power-law model is used and a good fit to the entire data set is achieved, the other models in Hayashida et al. (2012) do not account for the X-ray data because, as argued there, the X-rays do not correlate with the  $\gamma$ -ray and optical fluxes during flaring states. Their short variability model D2 requires an unexpectedly large energy density ( $\approx 10 \text{ erg cm}^{-3}$ ), so this model can be ruled out.

In the model by Sahayanathan & Godambe (2012), first-year Fermi data of 3C 279 (Abdo et al. 2010) is fit with  $\Gamma = 26, B' = 0.67 \text{ G}, u_{IR} = 4 \times 10^{-3} \text{ erg cm}^{-3}$ , an 860 K dust temperature, and a one-day variability time scale. Scattered accretion-disk radiation gives a similar emission component (Hartman et al. 2001; Dermer & Schlickeiser 2002) as IR radiation, so it is important to determine if the  $\gamma$ -ray emission region is made deep within the BLR or farther out, where the BLR radiation is more dilute. Here  $\gamma\gamma$  studies at the VHE regime can determine location.

### 6.4. Particle acceleration and the highest energy $\gamma$ rays

The log-parabola function, originally introduced because it gave good fits to the curving synchrotron SEDs of “active” (blazar-like) radio sources (Landau et al. 1986) and to the  $\gamma$ -ray spectra of Mrk 421 and Mrk 501 (Krennrich et al. 1999), has since been used to fit blazar (Giommi et al. 2002; Massaro et al. 2004) and gamma-ray burst (Massaro et al. 2010) spectra. It has also been recognized as a convenient functional form for the electron energy distribution (Massaro et al. 2006).

If a log-parabola nonthermal electron spectrum is capable of fitting multiwavelength blazar data reasonably well, as we have tried to demonstrate here, then one can ask about the physical processes that can generate such a distribution. Curving functions arise in second-order, stochastic acceleration scenarios (e.g., Park & Petrosian 1995; Becker et al. 2006; Tramacere et al. 2011). A turbulent scenario might also naturally arise in models involving relativistic shocks and jet reconnection in Poynting-dominated jet models and compact knots far ( $\gtrsim \text{pc}$ ) from the nucleus (e.g., Giannios et al. 2009; Nalewajko et al. 2012). The accelerated particle distribution is, however, poorly known, and dependent on

model assumptions.

With regard to the fits to 3C 279, the equipartition model underproduces the  $\gg$  GeV emission measured by *Fermi*-LAT in Epochs A, B, and C, but can be corrected with a long variability time, at the expense of fitting the X-ray data. The VHE detection of 3C 279 (MAGIC Collaboration 2008) would, however, have to require either emissions from leptons far out of equilibrium accompanied by poor fits to the X-ray or synchrotron data. Another possibility is hadronic processes to explain the  $\gamma$ -ray excess.

#### 6.5. Hadronic $\gamma$ rays in 3C 279 and UHECRs

In view of emission extending to the VHE range, which is hard to understand with leptonic models (Böttcher et al. 2009), a new spectral component may be required. A possible candidate is UHECRs accelerated in blazar jets. As we have seen, the jet powers can accommodate large baryon-load factors,  $\zeta_{p,nuc} \lesssim 20$ , so 3C 279 or indeed other powerful FSRQs, could display high-energy hadronic emission tails (Atoyan & Dermer 2003; Böttcher et al. 2009, 2013).

From the Hillas (1984) condition, the maximum particle energy is limited to energy  $E < E_{max} \cong Zce\delta_D^2 B' t_{var}$ . Using Equations (11) and (12), we find

$$E_{max}(\text{eV}) \cong 1.4 \times 10^{20} Z \frac{L_{48}^{5/16} t_4^{1/8} f_1^{1/4} f_2^{1/8}}{\zeta_e^{1/4} \zeta_s^{1/6} f_0^{1/16}}, \quad (31)$$

so equipartition blazars with sufficiently large apparent power can accelerate protons to ultra-high energies (Dermer & Razzaque 2010; Murase & Takami 2009). Thus 3C 279 could in principle accelerate protons to super-GZK energies by this basic requirement. FSRQs like 3C 279 are, however, unlikely to make all the UHECRs, because FSRQs are not found within the GZK radius of  $\sim 100 - 200$  Mpc. Moreover, in spite of their great power, the low space density of FSRQs and FR2 radio galaxies makes them unlikely to be the primary source class powering the UHECRs, compared to FR1 radio galaxies and BL Lac objects, which however have trouble to accelerate  $\gtrsim 10^{19}$  eV protons (Murase et al. 2012).

UHECR production in FSRQs like 3C 279 might be revealed by detection of steady, extended cascade radiation induced by photopion and photopair processes from beamed ultra-relativistic protons travelling through intergalactic space, as proposed to explain the spectra and variability properties of some unusual TeV BL Lac objects (Essey & Kusenko 2010; Essey et al. 2010; Essey & Kusenko 2012). Provided the UHECR beam can escape from the structured regions surrounding 3C 279 without being dispersed (Murase 2012), a slowly varying UHECR-induced  $\gamma$ -ray halo should surround 3C 279. The MAGIC detection of VHE emission from 3C 279 shows, however, VHE emission that possibly varies on timescales less than a day. Hadronic models considered by Böttcher et al. (2009) to fit the MAGIC VHE data require large powers. It remains to be seen if modifications of leptonic scenarios, for example, involving strongly magnetized jets and magnetic reconnection models in a multi-zone jets-within-jets-type model (Marscher & Jorstad 2010), or hadronic models with

proton synchrotron or photopion production and cascades (Böttcher et al. 2013), are preferred to make the VHE  $\gamma$ -ray spectra in 3C 279.

#### 6.6. External $\gamma\gamma$ Opacity and CTA

Expressions for  $\gamma\gamma \rightarrow e^\pm$  opacity (Gould & Schröder 1967; Brown, Mikaelian, & Gould 1973) applied to the inner-jet environment can be found in Dermer et al. (2012). For a monochromatic isotropic external radiation field, the  $\gamma\gamma$  opacity  $\tau_{\gamma\gamma}(\epsilon_1)$  reaches its maximum value  $\tau_{\gamma\gamma}^{max}(\epsilon_1^{max}) \cong 0.56 \times (3\sigma_T R/8m_e c^2 \epsilon_0)$  at  $\epsilon_1 \cong 3.54/\epsilon_0$ . For Ly  $\alpha$  photons, the  $\gamma\gamma$  opacity from an external radiation field therefore reaches its maximum for 90 GeV photons at the source, and the condition  $\tau_{\gamma\gamma} < 1$  implies an attenuation length  $\lambda_{\gamma\gamma}(\text{pc}) < 0.04/u_{-3}$ , where the BLR energy density is  $10^{-3}u_{-3}$  erg  $\text{cm}^{-3}$ . Detection of  $\approx 100$  GeV photons immediately puts the location of the  $\gamma$ -ray emission site far beyond  $r_{BLR}$ , depending on the value of  $\tau$  in Equation (28). Consequently the VHE  $\gamma$ -ray production sites in 3C 279 and 4C+21.35 are far outside the BLRs of these sources. External  $\gamma\gamma$  absorption effects should however be unimportant in the *Fermi* LAT spectrum of 3C 279, measured below  $\approx 10$  GeV.

The  $\gamma\gamma$  opacity constraint is even more severe for attenuation by infrared dust photons, though for higher energy  $\gamma$  rays. For a graybody radiation field with temperature  $m_e c^2 \Theta/k_B$  and energy density  $= 10^{-4}u_{-4}$  erg  $\text{cm}^{-3}$ , the opacity  $\tau_{\gamma\gamma}^{IR}$  reaches a maximum value of  $1.076 \times (45/8\pi^4)(\sigma_T R u_0/m_e c^2 \Theta)$  at  $\epsilon \cong 2/\Theta$ . For 1200 K dust, the attenuation length  $\lambda_{\gamma\gamma}(\text{pc}) \cong 0.01/u_{-4}$  for  $\approx 5$  TeV  $\gamma$  rays. Observations of VHE emissions in blazars with ground-based  $\gamma$ -ray telescope arrays and with the Cherenkov Telescope Array both at  $\approx 100$  GeV and multi-TeV energies will be important for confining the location of the  $\gamma$ -ray emission site.

#### 6.7. Blazar Correlations and Equipartition

Besides fitting individual spectra of a single blazar, the principle of equipartition holds promise for explaining blazar correlations such as the blazar sequence and blazar divide. The blazar sequence (Fossati et al. 1998; Ghisellini et al. 1998) refers to an inverse correlation of  $\gamma'_{pk}$  and  $L_\gamma$ , though later studies argue for additional complexity related to jet structure (Meyer et al. 2011) that can be explained in cooling scenarios (Finke 2013). The blazar divide refers to the correlation between the  $\gamma$ -ray spectral index and  $\gamma$ -ray luminosity (Abdo et al. 2010c; Ghisellini et al. 2009), and is closely related to the blazar sequence, as is the correlation of  $\gamma$ -ray spectral index with synchrotron  $\nu F_\nu$  peak frequency (Abdo et al. 2010c). The equipartition approach can predict trends and correlations in the statistics of blazars with, e.g.,  $t_{var}$ ,  $L_{syn}$ , and Compton dominance, that can be compared with data, and is currently under investigation.

## 7. SUMMARY

With the goal of minimizing the number of free parameters, we use a three-parameter log-parabola function for the electron distribution and assume equipartition between the energy densities of the magnetic field and nonthermal leptons ( $\zeta_e = 1$ ). On this basis, we derive Equations (11) – (13) giving  $\delta_D$ ,  $B'$ ,  $\gamma'_{pk}$ . The main

inputs from the data are  $\nu L_\nu^{pk, syn}$ , the peak value of the  $\nu L_\nu$  synchrotron spectrum,  $\nu_s$ , the frequency at which the  $\nu L_\nu$  synchrotron spectrum peaks, and  $t_{var}$ , the variability time scale. Using the equipartition assumption, values of  $\zeta_s$  and  $\zeta_*$ , which determine the SSC and external Compton-scattered  $\gamma$ -ray fluxes, are adjusted to fit the multiwavelength data.

We considered warm dust ( $T = 440$  K) and hot dust ( $T = 1200$  K) IR radiation fields, and assumed  $\theta = 1/\Gamma$  and  $t_{var} = 10^4$  s. From fits to 4 epochs of 3C 279, Ly $\alpha$  radiation energy densities  $\sim (0.2 - 2) \times 10^{-3}$  erg cm $^{-3}$  are derived, and IR energy densities a factor of a few smaller. These values are compatible with a  $\gamma$ -ray production site at the outer edge of the BLR,  $\gtrsim 0.1$  pc from the nucleus. If the variability time is longer than  $10^4$  s, the external field energy densities can be smaller and distance from the nucleus larger. The absolute jet powers are well below the Eddington limit unless the baryon-loading is  $\gtrsim 10$ , and somewhat larger than the accretion-disk luminosities used in the fits.

The inferred IR energy densities, ranging by about an order of magnitude for the four different epochs considered, are easier to explain if the  $\gamma$ -ray emission site is found in the same radial range where IR gradients take place. A location of the  $\gamma$ -ray emission site  $\approx 0.1 - 0.5$  pc from the nucleus is also consistent with relativistic shell collision radii.

We also find that protons satisfy the Hillas condition for acceleration above  $10^{20}$  eV for values of  $\delta_D$ ,  $B'$ , and

$r'_b$  derived in this model for the jets of 3C 279. Whether leptonic or hadronic processes make the  $\gg$  GeV radiation observed with *Fermi*-LAT and VHE radiation observed with MAGIC is not clear.

To summarize, this paper introduces a new blazar modeling technique based on equipartition between leptons and magnetic field, assuming the log-parabola form for the  $\gamma'^2 N'(\gamma')$  electron spectrum. We tested the method by fitting recent *Fermi*-LAT and multiwavelength data of 3C 279, deriving reasonable values for the broad-line and IR energy densities if the emission site is at  $\sim 0.1 - 0.5$  pc from the black hole, and the variability time is  $10^4$  s. Excess GeV radiation detected with the *Fermi*-LAT can be explained for larger variability times, but then the X-rays are not well fit. A sensitive MeV telescope would be valuable to determine the frequency of the peak and the contributions of scattered IR emission to the  $\gamma$ -ray spectrum of blazars. Searches for rapid variability of VHE  $\gamma$  rays from 3C 279 with imaging atmospheric Cherenkov gamma-ray telescopes, including the Cherenkov Telescope Array, will be crucial for finding the limits of leptonic models and potential signatures of hadrons.

We thank Dr. M. Hayashida for providing the 3C 279 data, and J. D. Finke and S. Razzaque for discussions. We thank the referee for an excellent and challenging report. The work of C.D.D. is supported by the Office of Naval Research and the NASA *Fermi* Guest Investigator Program.

## APPENDIX

### A. CORRECTIONS TO EQUIPARTITION RELATIONS

For an electron distribution with the log-parabola form given by  $\gamma'^2 N'_e(\gamma') = K x^{-b \log x}$  from Equation (1), with  $K = \gamma'^2_{pk} N'_e(\gamma'_{pk})$  and  $x = \gamma'/\gamma'_{pk}$ , we can derive a few elementary relations. First,

$$N_{e0} = \int_1^\infty d\gamma' N'_e(\gamma') = \frac{K}{\gamma'_{pk}} \left( \int_0^\infty dx x^{\hat{b} \ln x} - \int_{\gamma'_{pk}}^\infty dx x^{\hat{b} \ln x} \right) \equiv \frac{K}{\gamma'_{pk}} (I - I_e), \quad (\text{A1})$$

defining  $\hat{b} = b/\ln 10$ . Interestingly,

$$I = \int_0^\infty dx x^{-2-\hat{b} \ln x} = \int_0^\infty dx x^{-\hat{b} \ln x} = 10^{1/4b} \sqrt{\frac{\pi \ln 10}{b}} \quad (\text{A2})$$

Thus

$$K = \frac{N_{e0} \gamma'_{pk}}{I} = \frac{N_{e0} \gamma'_{pk} 10^{-1/4b}}{\sqrt{\pi \ln 10/b}} \equiv 2 N_{e0} \gamma'_{pk} f_3. \quad (\text{A3})$$

The fractional error incurred by letting  $\gamma'_{pk} \rightarrow 0$  in Equation (A1) is

$$\frac{I_e}{I} = \frac{1}{2} [1 - \text{erf}(u)] \xrightarrow{u \gg 1} \frac{\exp(-u^2)}{2u\sqrt{\pi}}, \quad (\text{A4})$$

where  $\text{erf}(u) \equiv \frac{2}{\sqrt{\pi}} \int_0^u dt \exp(-t^2)$  is the error function, and  $u = \sqrt{\hat{b}} \ln \gamma'_{pk} + 1/2\sqrt{\hat{b}}$ . The error is always small when  $\gamma'_{pk} \gg \exp \sqrt{1/\hat{b}}$  which, for typical values  $b \approx 1$  obtained in the fits, means that the correction is negligible when  $\gamma'_{pk} \gg 5$ .

The total nonthermal electron energy in the comoving fluid frame is

$$\mathcal{E}'_e = m_e c^2 \int_1^\infty d\gamma' \gamma' N'_e(\gamma') = K m_e c^2 \left( \int_{1/\gamma'_{pk}}^\infty dy y^{-1-\hat{b} \ln y} - \int_{\gamma'_{pk}}^\infty dy y^{-1-\hat{b} \ln x} \right) \equiv K (I_1 - I_{1e}). \quad (\text{A5})$$



It follows that

$$I_1 = \sqrt{\frac{\pi \ln 10}{b}} . \quad (\text{A6})$$

The fractional error  $I_{1e}/I_1$  incurred by letting  $\gamma'_{pk} \rightarrow 0$  is given by the right hand side of Equation (A4), except that now  $u = \sqrt{\hat{b}} \ln \gamma'_{pk}$ . When  $\gamma'_{pk} \gg \exp(1/\sqrt{\hat{b}})$ , this error is negligible. Comparison with values of  $b \approx 1$  and  $\gamma'_{pk} \gtrsim 20$  for the considered cases shows that neglecting the error correction is a good approximation.

### B. $\delta$ -FUNCTION SYNCHROTRON SPECTRUM FOR LOG-PARABOLA ELECTRON DISTRIBUTION

Here we go beyond the mono-energetic electron approximations for the equipartition relations, and include corrections for the width parameter  $b$  of the log-parabola function.

Beginning with the log-parabola electron distribution, Equation (1), and the comoving synchrotron luminosity from mono-energetic electrons,  $L'_{syn} = \frac{4}{3} c \sigma_T (B'/8\pi) \gamma'^2 N_{e0}$ , it is straightforward to derive

$$\epsilon L_{syn}(\epsilon) = v x^{1-\hat{b} \ln x} \quad (\text{B1})$$

for the spectral synchrotron luminosity. To obtain this result, we use the  $\delta$ -function approximation for the mean synchrotron photon energy,  $\epsilon'_{syn} = (3/2)(B'/B_{cr})\gamma'^2_{pk}$ , and the relation  $\epsilon' L_{syn}(\epsilon') = \gamma' L'_{syn}(\gamma')$ . Here  $x \equiv \sqrt{\epsilon'/\epsilon'_{pk}} = \sqrt{\epsilon'/\epsilon'_{pk}}$ , and  $\epsilon_{pk} = \delta_D \epsilon'_{pk} = (3/2)\delta_D (B'/B_{cr})\gamma'^2_{pk}$  is the peak synchrotron photon energy from a mono-energetic electron distribution with Lorentz factor  $\gamma'_{pk}$ . The upsilon coefficient

$$v \equiv K \delta_D^4 c \sigma_T \frac{B'^2}{12\pi} \gamma'_{pk} = L_{syn} f_3 , \quad (\text{B2})$$

using Equations (A3) and (A6), assuming negligible error.

The dimensionless peak frequency  $\epsilon_s$  of the  $\nu F_\nu$  synchrotron spectrum is obtained by taking the maximum of Equation (B1). One finds

$$\epsilon_s = f_2 \epsilon_{pk} , \quad f_2 \equiv 10^{1/b} . \quad (\text{B3})$$

The bolometric synchrotron luminosity, neglecting self-absorption corrections, is given by Equation (B1) through

$$L_{syn} = \int_0^\infty d\epsilon L_{syn}(\epsilon) = \frac{4}{3} c \sigma_T N_{e0} \delta_D^4 u'_{B'} \gamma'^2_{pk} = \frac{v}{f_3} . \quad (\text{B4})$$

Equation (6) for the synchrotron luminosity is recovered without correction. The relationship between  $L_{syn}$  and the  $\nu L_\nu$  peak synchrotron luminosity at  $\epsilon = \epsilon_s$  is

$$L_{syn} = 2 \sqrt{\frac{\pi \ln 10}{b}} \nu L_\nu^{pk, syn} , \quad (\text{B5})$$

so, from eq. (B2),

$$v \equiv 10^{-1/4b} \nu L_\nu^{pk, syn} . \quad (\text{B6})$$

Starting from Equation (6.60) in Dermer & Menon (2009) and using the  $\delta$ -function Thomson approximation (Equation (6.58)), which is exact in the Thomson limit, one can derive the ratio of the apparent SSC and synchrotron luminosities. We find

$$\frac{L_{SSC}}{L_{syn}} = \frac{\sigma_T N_{e0} \gamma'^2_{pk}}{3\pi r'_b{}^2 f_0} = \frac{\sigma_T \mathcal{E}'_e \gamma'_{pk}}{3\pi m_e c^4 \delta_D^2 t_{var}^2 f_0 f_1} = \frac{4}{3} \frac{c \sigma_T u'_e \gamma'_{pk}}{m_e c^2 f_1} . \quad (\text{B7})$$

### C. $\gamma\gamma$ OPACITY OF SYNCHROTRON RADIATION EMITTED BY LOG-PARABOLA ELECTRON DISTRIBUTION

Using Equation (B1) and the relation  $\epsilon L_{syn}(\epsilon) = \delta_D^4 \epsilon' L'_{syn}(\epsilon')$ , the comoving spectral photon density

$$n'(\epsilon') = \frac{\epsilon' u'(\epsilon')}{m_e c^2 \epsilon'^2} = \frac{v x^{1-\hat{b} \ln x}}{4\pi f_0 m_e c^3 r'_b{}^2 \epsilon'^2 \delta_D^4} . \quad (\text{C1})$$

The  $\gamma\gamma$  opacity for a photon with comoving energy  $\epsilon'_1 = \epsilon_1/\delta_D$  traveling through an emission region with characteristic size  $r'_b$  is

$$\tau_{\gamma\gamma}(\epsilon'_1) \cong r'_b \int_0^\infty d\epsilon' n'(\epsilon') \sigma_{\gamma\gamma}(\epsilon' \epsilon'_1) = \frac{v \sigma_T \epsilon'_1}{24\pi f_0 m_e c^4 t_{var} \delta_D^5} \hat{x}^{1-\hat{b} \ln \hat{x}} \equiv \mathcal{C} \hat{x}^{1-\hat{b} \ln \hat{x}} , \quad (\text{C2})$$

using the  $\delta$ -function approximation,  $\sigma_{\gamma\gamma}(\epsilon' \epsilon'_1) \cong 2\sigma_T \delta(\epsilon' \epsilon'_1 - 2)/3$ , for the  $\gamma\gamma$  cross section. Here  $\hat{x} = \sqrt{\epsilon'/\epsilon'_{pk}} = \sqrt{2/\epsilon'_1 \epsilon'_{pk}} = \delta_D \sqrt{2/\epsilon_1 \epsilon_{pk}}$ . The peak  $\gamma\gamma$  opacity occurs at  $\hat{x}_{max} = 10^{-1/2b}$ , or at photon energy  $\epsilon_{1,max} = 2\delta_D^2 10^{2/b}/\epsilon_s$ ,

as can be found by differentiating Equation (C2) with respect to  $\epsilon_1$ . Thus  $\tau_{\gamma\gamma}(\epsilon_1) = \tau_{\gamma\gamma,max}\hat{x}^{-3-\hat{b}\ln\hat{x}}$ , where  $\tau_{\gamma\gamma,max} = 10^{-1/4b}\mathcal{C}$ , and

$$\mathcal{C} = \frac{10^{-1/4b}\sigma_T\epsilon_1(\nu L_\nu^{pk, syn})}{24\pi m_e c^4 f_0 t_{var} \delta_D^6} \cong 1200\epsilon_1 \frac{10^{-1/4b}(\nu L_\nu^{pk, syn}/10^{48} \text{ erg s}^{-1})}{f_0 t_4 \delta_D^6}, \quad (\text{C3})$$

using Equation (B3). When  $\epsilon_1 \gg 1$ , the peak opacity can be large, depending on  $\delta_D$ , but only at very large photon energies, namely

$$E_{1,max} = m_e c^2 \epsilon_{1,max} \cong \frac{10^{17} \text{ eV}}{\nu_{14}} \left(\frac{\delta_D}{30}\right)^2 \left(\frac{10^{2/b}}{10^2}\right). \quad (\text{C4})$$

For the  $\gamma\gamma$  opacity of a photon in the SSC radiation field, Equation (C2) is used with  $\epsilon_s$  replaced by the peak SSC photon energy  $\epsilon_{SSC}$  where the  $\nu L_\nu$  SSC luminosity reaches its maximum value at  $\nu L_\nu^{pk, SSC}$ , and  $\nu L_\nu^{pk, syn}$  replaced by  $\nu L_\nu^{pk, SSC}$ . We assume that the log-parabola width parameter for the SSC SED spectrum is  $\approx b/2$ .

## REFERENCES

- Abdo, A. A., et al. 2009, *ApJ*, 699, 817  
— 2010a, *Nature*, 463, 919  
— 2010b, *ApJ*, 710, 1271  
— 2010c, *ApJ*, 715, 429  
Abdo, A. A., Ackermann, M., Agudo, I., et al. 2010, *ApJ*, 716, 30  
— 2011a, *ApJ*, 733, L26  
— 2011b, *ApJ*, 736, 131  
— 2011c, *ApJ*, 727, 129  
— 2011d, *ApJ*, 726, 43  
Abramowski, A., Acero, F., et al., H.E.S.S. Collaboration, 2013, *A&A*, 554, A107  
Ackermann, M., et al. 2010, *ApJ*, 721, 1383  
Aharonian, F., et al. 2007, *ApJ*, 664, L71  
Albert, J., Aliu, E., Anderhub, H., et al. 2007, *ApJ*, 669, 862  
Aleksić, J., et al. 2011, *ApJ*, 730, L8  
Aleksić, J., Antonelli, L. A., Antoranz, P., et al. 2011, *A&A*, 530, A4  
Arbeiter, C., Pohl, M., & Schlickeiser, R. 2002, *A&A*, 386, 415  
Atoyan, A. M., & Dermer, C. D. 2003, *ApJ*, 586, 79  
Beck, R., & Krause, M. 2005, *Astronomische Nachrichten*, 326, 414  
Becker, P. A., Le, T., & Dermer, C. D. 2006, *ApJ*, 647, 539  
Błażejowski, M., Sikora, M., Moderski, R., & Madejski, G. M. 2000, *ApJ*, 545, 107  
Brown, A. M. 2013, *MNRAS*, 431, 824  
Bonnoli, G., Ghisellini, G., Foschini, L., Tavecchio, F., & Ghirlanda, G. 2011, *MNRAS*, 410, 368  
Böttcher, M., Reimer, A., Sweeney, K., & Prakash, A. 2013, *ApJ*, 768,  
Böttcher, M., Harris, D. E., & Krawczynski, H. 2012, *Relativistic Jets from Active Galactic Nuclei* (Wiley: Weinheim)  
Böttcher, M., & Dermer, C. D. 2010, *ApJ*, 711, 445–454  
Böttcher, M., Reimer, A., & Marscher, A. P. 2009, *ApJ*, 703, 1168  
Böttcher, M. 2007, *Ap&SS*, 309, 95  
Böttcher, M., & Dermer, C. D. 2002, *ApJ*, 564, 86  
Böttcher, M., & Chiang, J. 2002, *ApJ*, 581, 127  
Brown, R. W., Mikaelian, K. O., & Gould, R. J. 1973, *Astrophysics Letters*, 14, 203  
Celotti, A., & Fabian, A. C. 1993, *MNRAS*, 264, 228  
Celotti, A., & Ghisellini, G. 2008, *MNRAS*, 385, 283  
Cerruti, M., Dermer, C. D., Lott, B., Boisson, C., & Zech, A. 2013, *ApJ*, 771, L4  
Collmar, W., Böttcher, M., Krichbaum, T. P., et al. 2010, *A&A*, 522, A66  
Cortina, J. 2012, *The Astronomer's Telegram*, 3965, 1  
Dermer, C. D., Schlickeiser, R., & Mastichiadis, A. 1992, *A&A*, 256, L27  
Dermer, C. D., & Schlickeiser, R. 1993, *ApJ*, 416, 458  
Dermer, C. D. 1995, *ApJ*, 446, L63  
Dermer, C. D., & Schlickeiser, R. 2002, *ApJ*, 575, 667  
Dermer, C. D., Finke, J. D., Krug, H., & Böttcher, M. 2009, *ApJ*, 692, 32; (e) 2012, *ApJ*, 747, 83  
Dermer, C. D., & Menon, G. 2009, *High Energy Radiation from Black Holes* (Princeton)  
Dermer, C. D., & Razaque, S. 2010, *ApJ*, 724, 1366  
Dermer, C. D., Murase, K., & Takami, H. 2012, *ApJ*, 755, 147  
Dermer, C. D., & Schlickeiser, R. 2002, *ApJ*, 575, 667  
Essey, W., & Kusenko, A. 2010, *Astroparticle Physics*, 33, 81  
Essey, W., Kalashev, O. E., Kusenko, A., & Beacom, J. F. 2010, *Physical Review Letters*, 104, 141102  
Essey, W., & Kusenko, A. 2012, *ApJ*, 751, L11  
Finke, J. D., Dermer, C. D., & Böttcher, M. 2008, *ApJ*, 686, 181  
Finke, J. D. 2013, *ApJ*, 763, 134  
Foschini, L., Ghisellini, G., Tavecchio, F., Bonnoli, G., & Stamerra, A. 2011, *A&A*, 530, A77+  
Fortson, L., VERITAS Collaboration, & Fermi-LAT Collaborators 2012, *American Institute of Physics Conference Series*, 1505, 514  
Fossati, G., Maraschi, L., Celotti, A., Comastri, A., & Ghisellini, G. 1998, *MNRAS*, 299, 433  
Georganopoulos, M., Kirk, J. G., & Mastichiadis, A. 2001, *ApJ*, 561, 111  
Ghisellini, G., Celotti, A., Fossati, G., Maraschi, L., & Comastri, A. 1998, *MNRAS*, 301, 451  
Ghisellini, G., & Celotti, A. 2001, *MNRAS*, 327, 739  
Ghisellini, G., Maraschi, L., & Dondi, L. 1996, *A&AS*, 120, 503  
Ghisellini, G., Maraschi, L., & Tavecchio, F. 2009, *MNRAS*, 396, L105  
Ghisellini, G., & Tavecchio, F. 2008, *MNRAS*, 387, 1669  
Giannios, D., Uzdensky, D. A., & Begelman, M. C. 2009, *MNRAS*, 395, L29  
Giommi, P., Capalbi, M., Fiocchi, M., et al. 2002, *Blazar Astrophysics with BeppoSAX and Other Observatories*, 63  
Gould, R. J. 1979, *A&A*, 76, 306  
Gould, R. J., & Schröder, G. P. 1967, *Phys. Rev.*, 155, 1404  
Gu, M., Cao, X., & Jiang, D. R. 2001, *MNRAS*, 327, 1111  
Hartman, R. C., et al. 1992, *ApJ*, 385, L1  
— 2001, *ApJ*, 553, 683  
Hayashida, M., et al. 2012, *ApJ*, 754, 114  
Hillas, A. M. 1984, *ARA&A*, 22, 425  
Jorstad, S. G., Marscher, A. P., Lister, M. L., et al. 2004, *AJ*, 127, 3115  
Jorstad, S. G., Marscher, A. P., Lister, M. L., et al. 2005, *AJ*, 130, 1418  
Jones, F. C. 1968, *Physical Review*, 167, 1159  
Katarzyński, K., Sol, H., & Kus, A. 2003, *A&A*, 410, 101  
Krennrich, F., Biller, S. D., Bond, I. H., et al. 1999, *ApJ*, 511, 149  
Lähteenmäki, A., & Valtaoja, E. 1999, *ApJ*, 521, 493  
Landau, R., Golisch, B., Jones, T. J., et al. 1986, *ApJ*, 308, 78  
MAGIC Collaboration, Albert, J., et al. 2008, *Science*, 320, 1752  
Malmrose, M. P., Marscher, A. P., Jorstad, S. G., Nikutta, R., & Elitzur, M. 2011, *ApJ*, 732, 116  
Marscher, A. P., & Jorstad, S. G. 2010, *arXiv:1005.5551*  
Marziani, P., Sulentic, J. W., Dultzin-Hacyan, D., Calvani, M., & Moles, M. 1996, *ApJS*, 104, 37  
Massaro, E., Perri, M., Giommi, P., & Nesci, R. 2004, *A&A*, 413, 489  
Massaro, E., Tramacere, A., Perri, M., Giommi, P., & Tosti, G. 2006, *A&A*, 448, 861  
Massaro, F., Grindlay, J. E., & Paggi, A. 2010, *ApJ*, 714, L299  
McNaron-Brown, K., Johnson, W. N., Jung, G. V., et al. 1995, *ApJ*, 451, 575  
Meyer, E. T., Fossati, G., Georganopoulos, M., & Lister, M. L. 2011, *ApJ*, 740, 98

- Mimica, P., & Aloy, M. A. 2012, MNRAS, 421, 2635
- Moderski, R., Sikora, M., & Błażejowski, M. 2003, A&A, 406, 855
- Murase, K., Dermer, C. D., Takami, H., & Migliori, G. 2012, ApJ, 749, 63
- Murase, K. 2012, ApJ, 745, L16
- Murase, K., & Takami, H. 2009, ApJ, 690, L14
- Nalewajko, K. 2013, MNRAS, 430, 1324
- Nalewajko, K., Begelman, M. C., Cerutti, B., Uzdensky, D. A., & Sikora, M. 2012, MNRAS, 425, 2519
- Nenkova, M., Sirocky, M. M., Ivezić, Ž., & Elitzur, M. 2008a, ApJ, 685, 147
- Nenkova, M., Sirocky, M. M., Nikutta, R., Ivezić, Ž., & Elitzur, M. 2008b, ApJ, 685, 160; (e) 2010, ApJ, 723, 1827
- Pacholczyk, A. G. 1970, Series of Books in Astronomy and Astrophysics, San Francisco: Freeman, 1970,
- Park, B. T., & Petrosian, V. 1995, ApJ, 446, 699
- Pian, E., Urry, C. M., Maraschi, L., et al. 1999, ApJ, 521, 112
- Poutanen, J., & Stern, B. 2010, ApJ, 717, L118
- Punch, M., et al. 1992, Nature, 358, 477
- Sahayanathan, S., & Godambe, S. 2012, MNRAS, 419, 1660
- Saito, S., Stawarz, L., Tanaka, Y. T., et al. 2013, ApJ, 766, L11
- Sari, R., Piran, T., & Narayan, R. 1998, ApJ, 497, L17
- Şentürk, G. D., Errando, M., Böttcher, M., & Mukherjee, R. 2013, ApJ, 764, 119
- Sikora, M., Begelman, M. C., & Rees, M. J. 1994, ApJ, 421, 153
- Sikora, M., Stawarz, L., Moderski, R., Nalewajko, K., & Madejski, G. M. 2009, ApJ, 704, 38
- Sokolov, A., & Marscher, A. P. 2005, ApJ, 629, 52
- Spada, M., Ghisellini, G., Lazzati, D., & Celotti, A. 2001, MNRAS, 325, 1559
- Stoeckle, J. T., Danforth, C. W., & Perlman, E. S. 2011, ApJ, 732, 113
- Stern, B. E., & Poutanen, J. 2011, MNRAS, 417, L11
- Tanaka, Y. T., et al. 2011, ApJ, 733, 19
- Tavecchio, F., & Ghisellini, G. 2012, arXiv:1209.2291
- Tramacere, A., Massaro, E., & Taylor, A. M. 2011, ApJ, 739, 66
- Wagner, S. J., Behera, B., & H.E.S.S. Collaboration. 2010, in Bulletin of the American Astronomical Society, Vol. 42, AAS/High Energy Astrophysics Division #11, 660
- Wehrle, A. E., et al. 1998, ApJ, 497, 178
- Woo, J.-H., & Urry, C. M. 2002, ApJ, 579, 530